Hadronic Light-by-Light Contribution to the Muon Anomalous Magnetic Moment

Institut für Kernphysik
Johannes Gutenberg-Universität Mainz

Masterarbeit

Nils Asmussen

Mainz, den 7. November 2013

Zusammenfassung

Der experimentell bestimmte Wert des anomalen magnetischen Moments des Myons weicht um drei Standardabweichungen von den Vorhersagen des Standardmodells ab. Die Hauptunsicherheit der theoretischen Vorhersage beruht auf dem Beitrag der hadronischen Licht-Licht-Streuung, der sich nicht auf Streuquerschnitte zurückführen lässt. Um sie dennoch zu berücksichtigen, stützt man sich auf gut erforschte Modelle. Der Beitrag des Pseudoskalar-Austausches dominiert den Beitrag zur Licht-Licht-Streuung, den nächstwichtigen Beitrag liefert die Pionschleife. Da der letztgenannte Anteil weniger genau bekannt ist, ist er der Hauptgegenstand dieser Masterarbeit. Der Beitrag der Pionschleife wird mit Hilfe von Dispersionsrelationen mit dem $\gamma\gamma \to \pi\pi$ Prozess, für den Messdaten existieren, verknüpft.
Beginnend mit der Lagrangedichte der skalaren Quantenelektrodynamik wurden die Born-Diagramme des $\gamma\gamma \to \pi\pi$ Prozesses für reelle und virtuelle Photonen abgeleitet und ausgewertet. Die notwendigen Korrekturen in der Kopplung zwischen Photonen und Pionen wurden mit einem Formfaktor berücksichtigt. Mit Hilfe des Optischen Theorems wird aus den Ergebnissen der Imaginärteil der $\gamma\gamma \to \gamma\gamma$ Amplitude hergeleitet. In der $\gamma^*\gamma^* \to \pi\pi$ Amplitude werden durch Unitarisierung der S und der D Partialwelle Mehrfachstreueffekte der Pionen im Endzustand berücksichtigt. Wie in der Arbeit gezeigt wird, stellt dies eine wesentliche Verbesserung dar und die resultierenden Streuquerschnitte liefern bis zur Kaon-Produktionsschwelle eine gute Beschreibung der Messdaten. Die Ergebnisse dieser Arbeiten werden u. a. dabei helfen, die BES III Daten zu analysieren und tragen insbesondere zum Verständnis von $\gamma^*\gamma^* \to \pi\pi$ als wichtigem Teil des hadronischen Licht-Licht Streuungsbetrags zum anomalen magnetischen Moment des Myons bei.

Contents

1 Introduction

In 1924, the Stern-Gerlach experiment [1] was the first to observe the magnetic moment $\boldsymbol{\mu}$. It was later defined as

$$\boldsymbol{\mu} = g\frac{e}{2m}\mathbf{S}\,,$$

where $\mathbf{S}$ is the spin of the particle with charge e and mass m, and the factor g is the Landé factor. By Dirac theory [2], the Landé factor of spin $\frac{1}{2}$-particles is predicted to be exactly 2.

With the development of particle accelerators and quantum field theory, deviations from Diracs prediction have been discovered. The magnetic moment $\boldsymbol{\mu}$ became a handy tool to validate the theory and to search for new physics. The deviation of the Landé factor g from the value 2 is called the anomalous magnetic moment a_l, where $l = e, \mu, \tau$ stands for the type of the lepton:

$$a_l = \frac{g_l - 2}{2}\,.$$

The first correction of this kind was published by Schwinger in 1948 [3] for the electron. The relevant diagram is

and leads to the first quantum correction to the anomalous magnetic moment of the lepton l

$$a_l = \frac{\alpha}{2\pi}\,.$$

For the muon, the theoretical and experimental values of a_μ are given in Tab. 1.1. From the theoretical side, there are many contributions to $g-2$. The most prominent of which are the quantum-electrodynamic (QED) corrections. Recently, they were investigated up to the fifth order in the coupling constant, leading to a very precise value of $a_\mu^{\mathrm{QED}} = 11\,658\,471.885(4)$ [4]. More than four orders of magnitude lower, there are hadronic vacuum polarization (HVP), hadronic light-by-light (HLBL), shown in Fig. 1.1(a), and electroweak (EW) corrections. Note that even though the values are much smaller than that of QED, the HVP and HLBL are the dominant sources of the theoretical uncertainty. Summing up the different contributions to the theoretical prediction, one sees that there are 3.4 standard deviations to the experimental result,

contribution	$a_\mu[10^{-10}]$		
QED (leptons)	11 658 471.885	$\pm$ 0.004	[4]
HVP (leading order)	692.3	$\pm$ 4.2	[5]
HVP (higher order)	$-$9.79	$\pm$ 0.07	[6]
HLBL	11.6	$\pm$ 4.0	[7]
EW	15.4	$\pm$ 0.2	[8]
total	11 659 181.4	$\pm$ 5.8	
experimental	11 659 208.0	$\pm$ 6.4	[9]

Table 1.1: Comparison of measured values for a_μ and theoretical predictions.

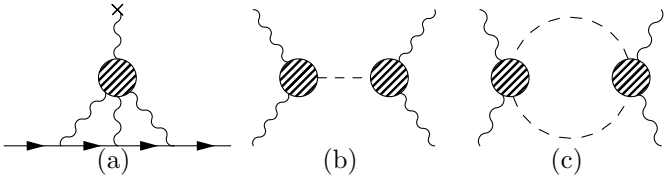

Figure 1.1: Hadronic light-by-light scattering contribution diagram (a), pseudo-scalar exchange dominant piece (b) and pion loop subdominant piece (c).

a difference that needs further investigation. There are two possible explanations: First, there is the possibility that by improving the calculations and measurements the deviation vanishes, or second, there could be yet unknown effects. In either case, it is very important to reduce the uncertainties of a_μ to be sure whether new physics is discovered or not.

It is proposed to measure the muon anomalous magnetic moment to a precision of 1.6×10^{-10} at FNAL [10]. This would be an improvement of the experimental uncertainty of roughly a factor of four. Obviously, the theoretical uncertainty also has to be improved by a similar amount to benefit from the planned measurements. As the theoretical uncertainty comes mostly from HVP and HLBL, their understanding has to be improved. By large-N_c (N_c being the number of colors) and by chiral counting, it was proposed in [11] to split the HLBL in the dominant pseudo-scalar exchange, Fig. 1.1(b), the subdominant pion-loop contribution, Fig. 1.1(c), and the quark-loop contribution. The second of which will be analyzed in this thesis.

The methods used in this thesis are explained in Chs. 2 to 6 and applied for the pion-loop contribution to the HLBL in Ch. 7, which contains the main results of this work. The detailed structure is as follows. The pion loop is related to the $\gamma\gamma \to \pi\pi$ process by dispersion relations and the optical theorem. The dispersion relations are introduced in Ch. 2, and allow to calculate the full invariant matrix element $\mathcal{M}$ from its imaginary part $\operatorname{Im}\mathcal{M}$. The imaginary part can be obtained by the optical theorem from $\gamma\gamma \to \pi\pi$ scattering. As this thesis makes use of the optical theorem, it is derived in Ch. 3 by exploiting the unitarity of the scattering matrix

S, that describes the time evolution for large times. To get a better understanding of the physics of the $\gamma\gamma \to \pi\pi$ process, the corresponding matrix elements are split into partial waves, as explained in Ch. 4. As it turns out, it is important for a precise description to include rescattering effects of the pions. A convenient way to accomplish this is to use the Omnès unitarization method, explained in Ch. 5, which preserves analyticity and crossing-symmetry. The last part which is needed to start the calculations are the Feynman rules. As this thesis deals with the low-energy behaviour of the HLBL, the calculations start from an effective Lagrangian for pions. The electromagnetic interactions are added to the free QED Lagrangian by the minimal substitution. The Feynman rules are then derived from the S matrix, as it is shown in Ch. 6. Chapter 7 is the main part of this thesis. It starts by a calculation of the HLBL for real photons using the optical theorem in Sec. 7.1, which is then validated through a direct derivation from the full Feynman diagrams in Sec. 7.2. The results are then decomposed into partial waves in Sec. 7.3. In Sec. 7.4.3, the optical theorem is applied to the more general case including virtual photons. The Sec. 7.5 incorporates rescattering effects in the final state by unitarizing the corresponding amplitude, which are important when comparing with data. At the end, Ch. 8 gives a short summary of this thesis and an outlook on what could be done further.

2 Dispersion Relations

In quantum field theory, one often has to deal with functions such as scattering matrix elements, which are analytic except for a branch cut singularity on the real axis, see Fig. 2.1. These singularities are a consequence of a propagation of on-shell intermediate states. It is often difficult to compute the whole function directly but much easier to derive its imaginary part. One way to do this is by using the optical theorem (see the discussion in the next chapter). Experimental data can also serve as input for such imaginary part. This is in deed used in Chapter 5 to improve on the analytic results of $\gamma\gamma \to \pi\pi$ scattering using measured $\pi\pi \to \pi\pi$ phase-shifts. Kramers and Kronig developped a technique [12, 13], that allows to reconstruct the full function under the knowledge of its imaginary part, the dispersion relations. The main ideas of their method are shown here.

Let $f(s)$ be a function with the following properties:

- It is analytic exept for a branch cut on the real axis for $s > s_0$.
- $\lim_{|s|\to\infty} sf(s) = 0$, so that the integration over the outer circle of the integration contour does not contribute (Jordan's lemma) [14].
- It fullfills the condition $f^*(s) = f(s^*)$.

The first condition ensures that Cauchy's integral formula can be used to integrate over the contour γ as shown in Fig. 2.1:

$$f(s) = \frac{1}{2\pi\imath} \int_\gamma \mathrm{d}s' \, \frac{f(s')}{s' - s} \, .$$

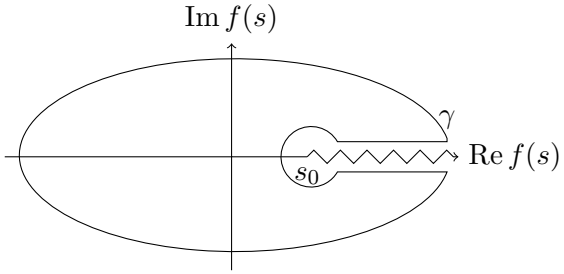

Figure 2.1: Integration contour γ in the complex plane for the derivation of the dispersion relation for a function $f(s)$ which has a branch cut on the real axis at $s > s_0$.

Using the second condition, this expression can be simplified as an integral over the discontinuity of $f(s)$ along the branch cut on the real axis. The third condition gives the relation $\mathrm{Disc}\, f(s) = 2\,\mathrm{Im}\, f(s+\imath\epsilon)$, where ϵ is a small positive number [15]. The formula, called unsubtracted dispersion relation, then reads:

$$f(s) = \frac{1}{\pi}\int_{s_0}^{\infty} \mathrm{d}s'\, \frac{\mathrm{Im}\, f(s'+\imath\epsilon)}{s'-s}\,. \tag{2.1}$$

In case $f(s)$ does not fulfill the Jordan's lemma, or if one wants to lessen the dependence on the imaginary part of $f(s)$ for high values of s, one can apply subtractions:

$$\frac{f(s)-f(0)}{s}\,.$$

The once subtracted dispersion relation is

$$f(s) = f(0) + \frac{s}{\pi}\int_{s_0}^{\infty} \mathrm{d}s'\, \frac{\mathrm{Im}\, f(s'+\imath\epsilon) - f(0+\imath\epsilon)}{s'(s'-s)}\,.$$

Note the extra s' in the denominator of the integrand.

3 Optical Theorem

The pion-loop HLBL is a process where one has two photons in the initial state and two photons in the final state and a pion loop as intermediate state. This obviously leads to a loop integration, which is done for real photons in Chapter 7.2. This process in the kinematics of a forward direction can also be viewed as two photons scattering to two pions and the pions scatter again to two photons — roughly speaking and ignoring the order, one has twice the process $\gamma\gamma \to \pi\pi$. The optical theorem, which will be explained in this chapter, concretizes the latter view. In the Born approximation, one only has to evaluate the trivial $\gamma\gamma \to \pi\pi$ Feynman diagram, which does not contain any loops. Then the optical theorem can be used to derive information about the $\gamma\gamma \to \gamma\gamma$ scattering, as it is done for real and virtual photons in Chapters 7.1 and 7.4, respectively. Another important benefit is, that it is possible to include experimental data into the calculations. For example, the unitarized $\gamma\gamma \to \pi\pi$ partial waves can serve as input to the optical theorem, as it is shown in Chapter 7.5.

The exact form of the optical theorem and its derivation are given in the following section.

3.1 Optical Theorem: Fundamentals

The optical theorem relates the imaginary part of forward scattering amplitudes to total cross sections. Since the optical theorem will play an important role in the present work, it is derived here similar to [15].

As the S-matrix is the limit of the unitary time evolution operator as time goes to infinity, it is also unitary:

$$\begin{aligned} 1 = S^\dagger S &= (1 - \imath T^\dagger)(1 + \imath T) \\ \Rightarrow -\imath \left(T - T^\dagger\right) &= T^\dagger T \,, \end{aligned} \tag{3.1}$$

where T is the interaction part of the S matrix.

To evaluate the matrix element $\mathcal{M}$ for a two to two scattering process with incoming particles with momenta $k_{1,2}$ and outgoing particles with momenta $p_{1,2}$ a complete set

of intermediate states with momenta $\{q_i\}$ is inserted on the right-hand side of (3.1):

$$\begin{aligned}
&-\imath\left[\mathcal{M}(k_1k_2\to p_1p_2)-\mathcal{M}^*(p_1p_2\to k_1k_2)\right]\delta^{(4)}\left(k_1+k_2-p_1-p_2\right)\\
&\quad=-\imath\left\langle p_1p_2\right|T-T^\dagger\left|k_1k_2\right\rangle\\
&\quad=\left\langle p_1p_2\right|T^\dagger T\left|k_1k_2\right\rangle\\
&\quad=\sum_n\left(\prod_{i=1}^n\int\frac{d^3q_i}{(2\pi)^3}\frac{1}{2E_i}\right)\left\langle p_1p_2\right|T^\dagger\left|\{q_i\}\right\rangle\left\langle\{q_i\}\right|T\left|k_1k_2\right\rangle\,.\\
&\quad=\sum_n\left(\prod_{i=1}^n\int\frac{d^3q_i}{(2\pi)^3}\frac{1}{2E_i}\right)\mathcal{M}^*(p_1p_2\to\{q_i\})\mathcal{M}(k_1k_2\to\{q_i\})\times\\
&\qquad(2\pi)^4\delta^{(4)}\left(k_1+k_2-\textstyle\sum_i q_i\right)(2\pi)^4\delta^{(4)}\left(k_1+k_2-p_1-p_2\right)\,.
\end{aligned}$$

This general formula leads to an expression for the forward scattering matrix element, the optical theorem. Therefor let $p_i=k_i$:

$$\begin{aligned}
\operatorname{Im}\mathcal{M}(k_1k_2\to k_1k_2)=&\frac{1}{2}\sum_n\left(\prod_{i=1}^n\int\frac{d^3q_i}{(2\pi)^3}\frac{1}{2E_i}\right)\left|\mathcal{M}(k_1k_2\to\{q_i\})\right|^2\times\\
&(2\pi)^4\delta^{(4)}\left(k_1+k_2-\textstyle\sum_i q_i\right)\\
=&2E_{\mathrm{cm}}p_{\mathrm{cm}}\sigma_{\mathrm{tot}}(k_1k_2\to\text{anything})\,,
\end{aligned}\tag{3.2}$$

where E_{cm} and p_{cm} are the center of mass (c. m.) energy and momentum, respectively.

Later, as this thesis deals with the pion-loop contribution, an intermediate state with two particles of mass m is needed. To specialize (3.2) to this case, the following calculations are done in the c. m. Let β and the squared c. m. energy s be defined:

$$\begin{aligned}
\beta=&\frac{|\mathbf{q}_1|}{E_1}\,,\\
s=&(k_1+k_2)^2\,.
\end{aligned}$$

Using (A.2), the delta function can be expressed in terms of these two quantities:

$$\begin{aligned}
\delta^{(4)}\left(k_1+k_2-q_1-q_2\right)=&\delta\left(\sqrt{s}-2\sqrt{\mathbf{q}_1^2+m^2}\right)\delta^{(3)}\left(\mathbf{k}_1+\mathbf{k}_2-\mathbf{q}_1-\mathbf{q}_2\right)\\
=&\delta\left(|\mathbf{q}_1|-\sqrt{\frac{s}{4}-m^2}\right)\frac{\sqrt{\mathbf{q}_1^2+m^2}}{2|\mathbf{q}_1|}\delta^{(3)}\left(\mathbf{q}_1+\mathbf{q}_2\right)\\
=&\frac{1}{2\beta}\delta\left(|\mathbf{q}_1|-\frac{\sqrt{s}}{2}\beta\right)\delta^{(3)}\left(\mathbf{q}_1+\mathbf{q}_2\right)\,.
\end{aligned}$$

Placing this again into (3.2), evaluating the integration over $\mathbf{q}_2$, and turning the remaining one into a spherical integral over $|\mathbf{q_1}|$ and the solid angle Ω_q, gives:

$$\operatorname{Im}M(k_1k_2\to k_1k_2)=\frac{\beta}{64\pi^2}\int\mathrm{d}\Omega_q\,M^*(k_1k_2\to q_1q_2)M(k_1k_2\to q_1q_2)\,.\tag{3.3}$$

4 Partial Wave Decomposition

Experimental data on the $\gamma\gamma \to \pi\pi$ process from the Mark II, Cello and Belle Collaboration is reported without a partial wave analysis. This means that a direct study of a resonance production is not possible. Rescattering effects of the intermediate pions depend also on their particular wave. To explore such effects, one needs to consider a partial wave decomposition.

The goal of this chapter is to explain such decomposition of the invariant matrix element M^{Λ} into partial wave amplitudes $B_{J\Lambda}(s)$, depending on the squared c. m. energy s, the total angular momentum J and its z-component Λ. The partial wave amplitudes describe the matrix element in a basis proportional to the associated Legendre polynomials $P_J^{\Lambda}(\cos\theta)$, which give the angular dependance. Note that they only depend on the c. m. polar angle θ but not on the azimuth angle. This is due to rotational symmetry. The decomposition leads to a deeper understanding of the physics (such as resonance production and rescattering effects) by splitting into the so called S, P, D, F, G, ... waves or orbitals. In Chapter 5 partial waves will be used to improve on $\gamma\gamma \to \pi\pi$ scattering amplitudes using measured phase-shifts of $\pi\pi \to \pi\pi$.

To motivate the decomposition, the main steps of the derivation for a simpler problem are shown [16]: Assume the scattering of a non-relativistic single particle scattering in a radially symmetric potential $V(r)$. The momentum $\mathbf{k}$ of the particle is expressed in the spherical wave basis $|Elm\rangle$ with energy E, angular momentum l and its z component m as

$$\langle \mathbf{k}|Elm\rangle = g_{lE}(|\mathbf{k}|)Y_l^m(\hat{\mathbf{k}})\,,$$

where $g_{lE}(|\mathbf{k}|)$ can be determined using the following relation with the free Hamilton operator H_0:

$$\begin{aligned}(H_0 - E)\,|Elm\rangle &= 0\\ \Rightarrow(\frac{\mathbf{k}^2}{2m} - E)\,\langle \mathbf{k}|Elm\rangle &= 0\,.\end{aligned}$$

Because the $\langle \mathbf{k}|Elm\rangle$ is in general not zero, the prefactor has to be zero, which is ensured by a delta function:

$$g_{lE}(|\mathbf{k}|) = N\delta\left(\frac{\mathbf{k}^2}{2m} - E\right)\,,$$

where N is a normalization constant. The intermediate result is

$$\langle \mathbf{k}|Elm\rangle = N\delta\left(\frac{\mathbf{k}^2}{2m} - E\right)Y_l^m(\hat{\mathbf{k}})\,.$$

The scattering amplitude is proportional to

$$\begin{aligned}\langle \mathbf{k}|T|\mathbf{k}\rangle &= \sum_{lml'm'} \int \mathrm{d}E \int \mathrm{d}E' \ \langle \mathbf{k}'|E'l'm'\rangle \langle E'l'm'|T|Elm\rangle \langle Elm|\mathbf{k}\rangle \\ &\propto \sum_{lm} T_l(E)\Big|_{E=\frac{\mathbf{k}^2}{2m}} Y_l^m(\hat{\mathbf{k}}')Y_l^m(\hat{\mathbf{k}})\,.\end{aligned}$$

The coordinate system can now be aligned so that $\mathbf{k}$ points in positive z direction. Then the spherical waves become:

$$\begin{aligned}Y_l^m(\hat{\mathbf{k}}) &= \sqrt{\frac{2l+1}{4\pi}}\delta_{m0}\,, \\ Y_l^0(\hat{\mathbf{k}}') &= \sqrt{\frac{2l+1}{4\pi}}P_l^0(\cos\theta)\,.\end{aligned}$$

That means that the scattering amplitude is proportional to a product of the energy dependent partial wave amplitude $T_l(E)$ and on a term giving the angular dependence, which is proportional to the Legendre polynomials $P_l^0(\cos\theta)$.

A similar relation is now valid for the decomposition into J and Λ for the (relativistic) two to two scattering matrix element. It reads:

$$\imath\mathcal{M}^\Lambda = 2\imath e^2 \sum_{J\geq 2} \sqrt{2J+1}\sqrt{\frac{(J-\Lambda)!}{(J+\Lambda)!}}P_J^\Lambda(\cos\theta)B_{J\Lambda}(s)\,. \tag{4.1}$$

In the case of $\gamma\gamma \to \pi\pi$ scattering, Λ is the difference of the photon helicities (see Sec. 7.1). Note the split into functions which give the angular dependence (the associated Legendre polynomials) and an amplitude giving the strength of that wave as function of the squared c. m. energy s.

By exploiting the orthogonality relation

$$\int_{-1}^{1} \mathrm{d}\cos\theta \sqrt{2J'+1}\sqrt{\frac{(J'+\Lambda)!}{(J'-\Lambda)!}}P_{J'}^\Lambda(\cos\theta) \times \sqrt{2J+1}\sqrt{\frac{(J+\Lambda)!}{(J-\Lambda)!}}P_J^\Lambda(\cos\theta) = 2\delta_{JJ'}\,,$$

the equation (4.1) can be solved for the partial wave amplitudes:

$$B_{J\Lambda} = \frac{1}{4\imath e^2}\int_{-1}^{1} d\cos\theta \sqrt{2J+1}\sqrt{\frac{(J-\Lambda)!}{(J+\Lambda)!}}P_J^\Lambda(\cos\theta)\mathcal{M}^\Lambda\,.$$

5 Omnès Unitarization Method

In Chapter 7, the partial waves for $\gamma\gamma \to \pi\pi$ will be derived from an effective Lagrangian in the Born approximation. Even though the Born approximation is the leading contribution at low energies, there are other effects that should be taken into account. The most important one is the rescattering effect of the intermediate pions. In this thesis, this is implemented through the Omnès unitarization method, which is the simplest one that satisfies crossing-symmetry and analyticity.

The unitarity condition [17] is

$$\operatorname{Im} F^I_{J\Lambda}(\gamma\gamma \to \pi\pi) = \sum_n \rho_n F^{I*}_{J\Lambda}(\gamma\gamma \to n)\mathcal{I}^I_J(n \to \pi\pi)\,,$$

where ρ_n denotes the kinematical and isospin factors and $\mathcal{I}(n \to \pi\pi)$ the hadronic amplitude and $F^I_{J\Lambda}$ the $\gamma\gamma \to \pi\pi$ amplitude with isospin I. The information this condition provides is, that the $\gamma\gamma \to \pi\pi$ and $\pi\pi \to \pi\pi$ partial waves have the same phase-shifts δ^I_J below the kaon-threashold.

The Born $\gamma\gamma \to \pi\pi$ partial wave amplitudes $B^I_{J\Lambda}(s)$ have a branch cut on the negative real axis. The amplitude $F^I_{J\Lambda}$, however, has a branch cut on the positive real axis above the pion production threshold. This branch cut is implemented by the Omnès function $\Omega^I_J(s)$ [18], which is related to the $\pi\pi \to \pi\pi$ phase-shifts:

$$\begin{aligned}
\Omega^I_J(s) &= \exp\left[\frac{s}{\pi}\int_{s_0}^{\infty} \mathrm{d}s'\, \frac{\delta^I_J(s')}{s'(s'-s-\imath\epsilon)}\right] \\
&= \exp\left[\frac{s}{\pi}\int_{s_0}^{\infty} \mathrm{d}s'\, \frac{\delta^I_J(s')-\delta^I_J(s)}{s'(s'-s-\imath\epsilon)} + \frac{s}{\pi}\int_{s_0}^{\infty} \mathrm{d}s'\, \frac{\delta^I_J(s)}{s'(s'-s-\imath\epsilon)}\right] \\
&= \exp\left[\frac{s}{\pi}\int_{s_0}^{\infty} \mathrm{d}s'\, \frac{\delta^I_J(s')-\delta^I_J(s)}{s'(s'-s)} + \frac{\delta^I_J(s)}{\pi}\ln\left(\frac{s_0}{s_0-s}\right)\right]\,. \qquad (5.1)
\end{aligned}$$

As can be seen from this relation, the Omnès function has a branch cut on the positive real axis with the correct phase for the unitarized partial wave amplitudes $F^I_{J\Lambda}$.

Now, a dispersion relation for $F^I_{J\Lambda}$ is constructed. Therefore the following function is written down:

$$\frac{\left(F^I_{J\Lambda}(s) - B^I_{J\Lambda}(s)\right)}{s(s-s_0)^{\frac{J}{2}}} \times \Omega^I_J(s)\,.$$

The function has the correct high energy behaviour needed, cf. Chapter 2, and it gives the correct phase for $F^I_{J\Lambda}$. This expression then enters in a dispersion relation, Eq. (2.1), and is evaluated by subtracting the integrand at the pole:

$$\begin{aligned} F^I_{J\Lambda}(s) = \Omega^I_J(s)\Bigg\{ & B^I_{J\Lambda}(s)\,\mathrm{Re}\left[(\Omega^I_J)^{-1}(s)\right] - \frac{s(s-s_0)^{\frac{J}{2}}}{\pi}\fint_{s_0}^{\infty}\mathrm{d}s'\,\frac{B^I_{J\Lambda}(s')\,\mathrm{Im}(\Omega^I_J)^{-1}(s)}{(s'-s_0)^{\frac{J}{2}}(s'-s)}\Bigg\} \\ = \Omega^I_J(s)\Bigg\{ & B^I_{J\Lambda}(s)\,\mathrm{Re}\left[(\Omega^I_J)^{-1}(s)\right] + \mathrm{Im}\left[(\Omega^I_J)^{-1}(s)\right]\frac{1}{\pi}\ln\left(\frac{s-s_0}{s_0}\right) \\ & - \frac{s(s-s_0)^{\frac{J}{2}}}{\pi}\int_{s_0}^{\infty}\frac{\mathrm{d}s'}{s'(s'-s)}\left(\frac{B^I_{J\Lambda}(s')\,\mathrm{Im}(\Omega^I_J)^{-1}(s')}{(s'-s_0)^{\frac{J}{2}}} - \frac{B^I_{J\Lambda}(s)\,\mathrm{Im}(\Omega^I_J)^{-1}(s)}{(s-s_0)^{\frac{J}{2}}}\right)\Bigg\}. \end{aligned} \tag{5.2}$$

Eq. (5.2) is the master formula for computing the partial waves from the $\pi\pi$-phase shifts and Born amplitudes.

6 Feynman Rules for Scalar Quantum Electrodynamics

The pion-loop HLBL will be calculated for low energies. In this chapter the Feynman rules needed for the HLBL will be calculated from an effective Lagrangian. As, in an effective theory, pions are scalar particles the derivation starts from the free scalar QED Lagrangian. The description of the electromagnetic interaction is then added through the minimal substitution. Then the scattering matrix S is built with the Lagrangian and finally, using the Wick theorem, the Feynman rules are derived from S.

The scalar QED Lagrangian of the free field is

$$\mathcal{L} = (\partial_\mu \Phi)^\dagger \, (\partial^\mu \Phi) - m^2 \Phi^\dagger \Phi \,,$$

where Φ is the pion field and m the pion mass. Using the minimal substitution

$$\partial_\mu \to D_\mu = \partial_\mu - \imath e A_\mu \,,$$

where D_μ denotes the covariant derivative, e the elementary (positive) charge and A_μ the electromagnetic vector potential, one can describe the electromagnetic interaction Lagrangian as

$$\begin{aligned} \mathcal{L}_I =& (D_\mu \Phi)^\dagger \, (D^\mu \Phi) \\ =& (\partial_\mu + \imath e A_\mu) \, \Phi^\dagger \, (\partial^\mu - \imath e A^\mu) \, \Phi \\ =& (\partial_\mu \Phi^\dagger)(\partial^\mu \Phi) \underbrace{- \imath e A_\mu ((\partial^\mu \Phi^\dagger)\Phi - \Phi^\dagger (\partial^\mu \Phi))}_{=:\mathcal{L}_1} + \underbrace{e^2 A_\mu A^\mu \Phi^\dagger \Phi}_{=:\mathcal{L}_2} \,. \end{aligned} \tag{6.1}$$

Here two different interaction contributions $\mathcal{L}_1$, that represents the $\gamma\pi\pi$ vertex, and $\mathcal{L}_2$, the $\gamma\gamma\pi\pi$ vertex are differentiated.

For a general process, the S-matrix element is

$$S = \sum_{k=0}^{\infty} \int d^4 x_1 \cdots \int d^4 x_k \, \frac{\imath^k}{k!} T \left[\mathcal{L}(x_1) \cdots \mathcal{L}(x_k) \right] \,,$$

where T is the time ordering operator. For the derivation of the Feynman rules the summand where $k = 1$ of the S matrix is needed, which will be called $S^{(1)}$:

$$S^{(1)} = \imath \int d^4 x \, T[\mathcal{L}_1(x) + \mathcal{L}_2(x)] =: S_1^{(1)} + S_2^{(1)} \,.$$

Finally, using the Wick theorem, one gets the Feynman rules:

$$\langle p,p'|\, S_1^{(1)}\, |q\rangle = \langle p,p'| - \imath \int d^4x\, e(\imath\partial^\mu \Phi^\dagger)\Phi A^\mu\, |q\rangle + \langle p,p'|\, \imath \int d^4x\, e\Phi^\dagger(\underbrace{\imath\partial^\mu}_{=\hat{p}^\mu}\Phi)A^\mu\, |q\rangle\,,$$

represented diagramatically as

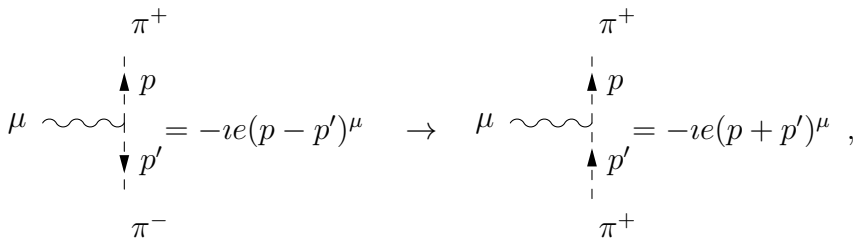

which corresponds at first order with $\mathcal{L}_1$ and

$$\langle p,p'|\, S_2^{(1)}\, |q,q'\rangle = \langle p,p'| \int d^4x\, \imath e^2 g^{\mu\nu}\Phi^\dagger\Phi A_\mu A_\nu\, |q,q'\rangle + \langle p,p'| \int d^4x\, \imath e^2 g^{\mu\nu}\Phi^\dagger\Phi A_\nu A_\mu\, |q,q'\rangle\,,$$

represented by

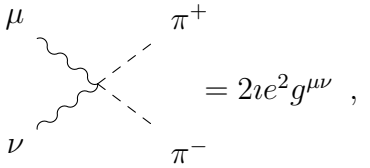

corresponding to $\mathcal{L}_2$.

With the corresponding Feynman rules derived, one can proceed to calculate the $\gamma\gamma \to \pi\pi$ process.

7 Hadronic Light-by-Light Scattering

In this chapter, the pion-loop HLBL will be studied in the Born approximation for real and virtual photons. There are effects beyond the Born approximation, the most important are accounting for the pion rescattering effects. The subprocess $\gamma^*\gamma^* \to \pi\pi$ will be modified to include them.

The chapter is divided as follows. In Sec. 7.1, the optical theorem is applied and validated by a direct evaluation of the Feynman diagrams in Sec. 7.2. The result is decomposed into partial waves and further analyzed Sec. 7.3. In Sec. 7.4, the same techniques are applied to the more general case which considers virtual photons. The calculations up to this point are given in the Born approximation and are, in Sec. 7.5, improved by including rescattering effects for the $\gamma^*\gamma^* \to \pi\pi$ scattering.

7.1 Hadronic Light-by-Light by the Optical Theorem

The imaginary part of the light-by-light scattering amplitude will be computed. Therefore, the Born diagrams for the process $\gamma\gamma \to \pi\pi$ are evaluated and then combined using the optical theorem.

7.1.1 Born Diagrams for $\gamma\gamma \to \pi\pi$

The leading order contribution to the process $\gamma\gamma \to \pi\pi$ at low energy is given by the Born diagrams that are shown in Fig. 7.1. Note that the Born diagrams only contain scattering to the charged pions, as the photons can only couple to charge. The corresponding matrix element is:

$$\imath\mathcal{M}^{\mathrm{BORN}} = \imath\mathcal{M}_a + \imath\mathcal{M}_b + \imath\mathcal{M}_c\,.$$

With the polarization vectors ϵ and ϵ' and momenta q and q' of the photons and the momenta p_{π^+}, p_{π^-} for the π^+ and π^- respectively, one can express the matrix

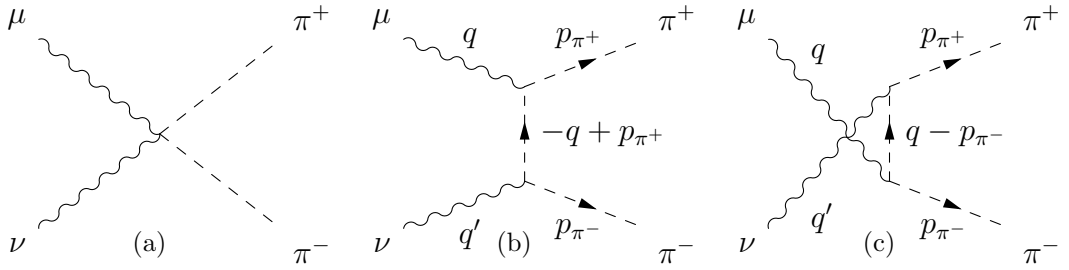

Figure 7.1: Born diagrams for the $\gamma\gamma \to \pi\pi$ process

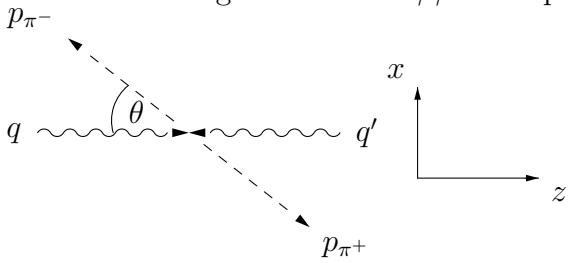

Figure 7.2: Kinematics of the process $\gamma\gamma \to \pi\pi$ in the center of mass frame.

elements as:

$$
\begin{aligned}
\imath\mathcal{M}_a =& \epsilon_\mu \epsilon'_\nu 2\imath e^2 g^{\mu\nu} = 2\imath e^2 \left(\epsilon \cdot \epsilon'\right) \,, \\
\imath\mathcal{M}_b =& \epsilon'_\nu \left(-\imath e\right) \left(-p_{\pi^-} - q + p_{\pi^+}\right)^\nu \frac{\imath}{\left(-q + p_{\pi^+}\right)^2 - m^2 + \imath\epsilon} \epsilon_\mu \left(-\imath e\right) \left(-q + p_{\pi^+} + p_{\pi^+}\right)^\mu \\
=& -2\imath e^2 \frac{1}{q p_{\pi^+}} \left(\epsilon \cdot p_{\pi^+}\right) \left(\epsilon' \cdot p_{\pi^-}\right) \,, \\
\imath\mathcal{M}_c =& \epsilon_\mu \left(-\imath e\right) \left(-p_{\pi^-} + q - p_{\pi^-}\right)^\mu \frac{\imath}{\left(q - p_{\pi^-}\right)^2 - m^2 + \imath\epsilon} \epsilon'_\mu \left(-\imath e\right) \left(q - p_{\pi^-} + p_{\pi^+}\right)^\nu \\
=& -2\imath e^2 \frac{1}{q p_{\pi^-}} \left(\epsilon \cdot p_{\pi^-}\right) \left(\epsilon' \cdot p_{\pi^+}\right) \,.
\end{aligned}
$$

In the center of mass system, as shown in Fig. 7.2, the kinematics of the process are defined as

$$
\begin{aligned}
q \cdot p_{\pi^\pm} =& E_q E_p \mp |\vec{q}||\vec{p}| \cos\theta \\
=& \frac{\sqrt{s}}{2}\frac{\sqrt{s}}{2} \mp \frac{\sqrt{s}}{2}|\vec{p}| \cos\theta \\
=& \frac{s}{4}\left(1 \mp \beta \cos\theta\right) \,,
\end{aligned}
$$

where s is the Mandelstam variable

$$
s = \left(q + q'\right)^2 \,,
$$

and β is defined as

$$
\beta = \sqrt{1 - \frac{4m_\pi^2}{s}} \,.
$$

Let Λ be the difference of the helicities λ and λ' of the two photons:

$$\Lambda = \lambda - \lambda' \,.$$

When both photons have the same helicity, $\Lambda = 0$, one can choose

$$\epsilon = \left(0, -\frac{1}{\sqrt{2}}, -\frac{\imath}{\sqrt{2}}, 0\right) \,, \quad \epsilon' = \left(0, +\frac{1}{\sqrt{2}}, -\frac{\imath}{\sqrt{2}}, 0\right) \,,$$

and the matrix elements become

$$\begin{aligned}
\imath\mathcal{M}_a^{\Lambda=0} =& 2ie^2 \,, \\
\imath\mathcal{M}_b^{\Lambda=0} =& 2ie^2 \frac{1}{\frac{s}{4}(1-\beta\cos\theta)} \frac{|\vec{p}|^2 \sin^2\theta}{2} \,, \\
\imath\mathcal{M}_c^{\Lambda=0} =& 2ie^2 \frac{1}{\frac{s}{4}(1+\beta\cos\theta)} \frac{|\vec{p}|^2 \sin^2\theta}{2} \,, \\
\imath\mathcal{M}_{\text{BORN}}^{\Lambda=0} =& 2\imath e^2 \frac{(1-\beta^2)}{1-\beta^2\cos^2\theta} \,.
\end{aligned}$$

And the same for opposite helicities, $\Lambda = 2$,

$$\epsilon = \left(0, -\frac{1}{\sqrt{2}}, -\frac{\imath}{\sqrt{2}}, 0\right) \,, \quad \epsilon' = \left(0, -\frac{1}{\sqrt{2}}, -\frac{\imath}{\sqrt{2}}, 0\right) \,,$$

$$\begin{aligned}
\imath\mathcal{M}_a^{\Lambda=2} =& 0 \,, \\
\imath\mathcal{M}_b^{\Lambda=2} =& 2\imath e^2 \frac{1}{\frac{s}{4}(1-\beta\cos\theta)} \frac{|\vec{p}|^2 \sin^2\theta}{2} \,, \\
\imath\mathcal{M}_c^{\Lambda=2} =& 2\imath e^2 \frac{1}{\frac{s}{4}(1+\beta\cos\theta)} \frac{|\vec{p}|^2 \sin^2\theta}{2} \,, \\
\imath\mathcal{M}_{\text{BORN}}^{\Lambda=2} =& 2\imath e^2 \frac{\beta^2 \sin^2\theta}{1-\beta^2\cos^2\theta} \,.
\end{aligned}$$

Notice that the contact diagram, Fig. 7.1(a), does not contribute when the photons have opposite helicities.

7.1.2 Fish, Triangle and Box Diagrams

The imaginary part of the light-by-light scattering, represented as

Im 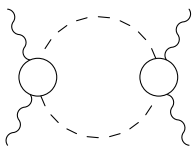 ,

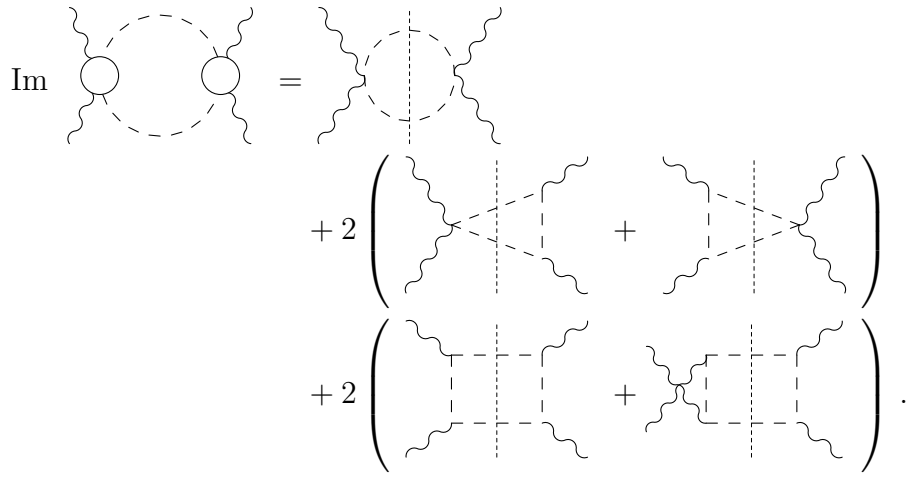

Figure 7.3: Optical theorem for the light-by-light scattering.

can be split in different contributions, see Fig. 7.3. Then, using the optical theorem, one sees that only the diagrams in the last line of the figure will contribute when $\Lambda = 2$, because all others contain the contact diagram.

Starting with Eq. (3.3), the amplitude takes the form

$$\mathrm{Im}\,\mathcal{M}_{\gamma\gamma\to\gamma\gamma} = \frac{\beta}{64\pi^2}\int d\Omega_{\pi_1}\left[\mathcal{M}_{\gamma\gamma\to\pi\pi}\right]\left[\mathcal{M}_{\gamma\gamma\to\pi\pi}\right]^* .$$

The first piece in Fig. 7.3, called the fish diagram, can be sketched as

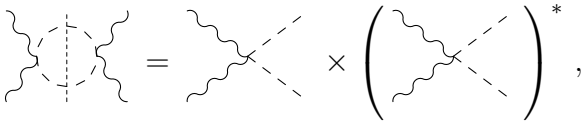

and evaluates to

$$\mathrm{Im}\,\mathcal{M}^{\text{fish}}_{\gamma\gamma\to\gamma\gamma} = \begin{cases} \frac{\beta e^4}{8\pi}\times 2 & \text{for } \Lambda = 0 \\ 0 & \text{else} \end{cases} . \tag{7.1}$$

The second line of Fig. 7.3 is called the triangle diagram

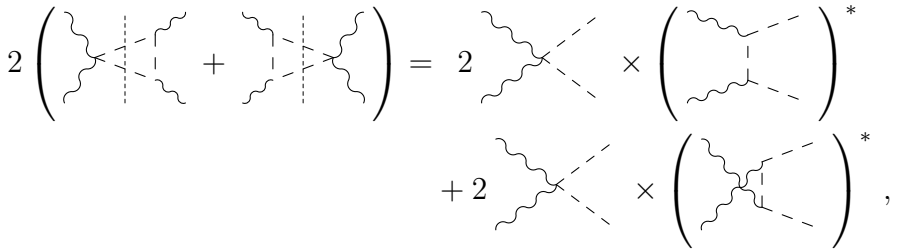

and the calculation yields

$$\operatorname{Im}\mathcal{M}^{\text{triangle}}_{\gamma\gamma\to\gamma\gamma} = \begin{cases} \frac{\beta e^4}{8\pi}\left(-4+\frac{2(1-\beta^2)}{\beta}\ln\left(\frac{1+\beta}{1-\beta}\right)\right) & \text{for } \Lambda = 0 \\ 0 & \text{else} \end{cases} . \tag{7.2}$$

Finally, the diagram from the last line of Fig. 7.3, called the box diagram,

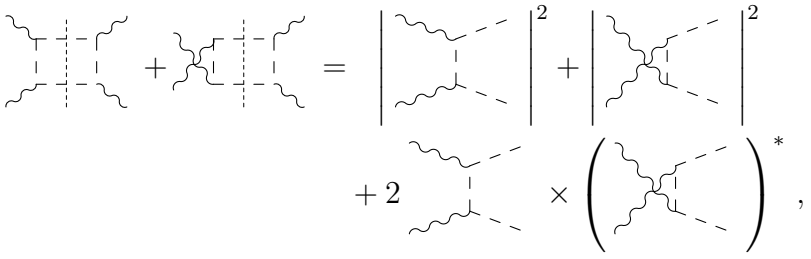

gives

$$\operatorname{Im}\mathcal{M}^{\text{box}}_{\gamma\gamma\to\gamma\gamma} = \frac{\beta e^4}{8\pi}\left(3-\beta^2-\frac{(1-\beta^2)(3+\beta^2)}{2\beta}\ln\left(\frac{1+\beta}{1-\beta}\right)\right) . \tag{7.3}$$

This result is the same for $\Lambda = 0$ and $\Lambda = 2$.

Gathering the different results in Eqs. (7.1), (7.2) and (7.3), the complete imaginary part of the Born matrix element is

$$\operatorname{Im}\mathcal{M}^{\text{BORN}} = \frac{\beta e^4}{8\pi} \times \begin{cases} (1-\beta^2)\left\{1+\frac{1-\beta^2}{2\beta}\ln\left(\frac{1+\beta}{1-\beta}\right)\right\} & \text{for } \Lambda = 0 \\ 3-\beta^2-\frac{(1-\beta^2)(3+\beta^2)}{2\beta}\ln\left(\frac{1+\beta}{1-\beta}\right) & \text{else} \end{cases} . \tag{7.4}$$

As mentioned above, only the box diagrams contribute to the imaginary part of the $\gamma\gamma \to \gamma\gamma$ matrix element when $\Lambda = 2$, while in the other case, $\Lambda = 0$, all diagrams contribute.

7.2 Calculation of the Feynman Diagrams

To ensure that the results from the previous section are correct, the $\gamma\gamma \to \gamma\gamma$ process is now evaluated again in an independent way by directly calculating the imaginary part of the forward scattering amplitude from the full diagrams using the Feynman techniques.

7.2.1 Fish Diagram

The matrix element corresponding to the fish diagram shown in Fig. 7.4 is:

$$\begin{aligned} \imath\mathcal{M} &= \int \frac{d^4p}{(2\pi)^4}\epsilon_{1,\mu}\epsilon_{2,\nu}\, 2\imath e^2 g^{\mu\nu}\, \frac{\imath}{(p+q_1+q_2)^2-m_\pi^2+\imath\epsilon}\, 2\imath e^2 g^{\sigma\rho}\, \frac{\imath}{p^2-m_\pi^2+\imath\epsilon}\, \epsilon_{4,\sigma}\epsilon_{3,\rho} \\ &= (\epsilon_1\cdot\epsilon_2)\,(\epsilon_3\cdot\epsilon_4)\, 4e^4 \int \frac{d^4p}{(2\pi)^4}\frac{1}{(p+q_1+q_2)^2-m_\pi^2+\imath\epsilon}\frac{1}{p^2-m_\pi^2+\imath\epsilon} , \end{aligned}$$

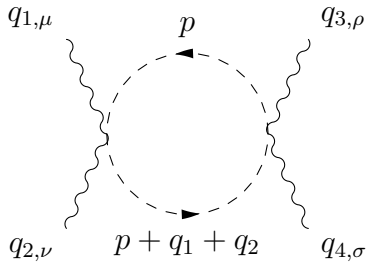

Figure 7.4: Fish diagram for light-by-light scattering with a charged pion loop.

where the ϵ_i are the polarization vectors of the photons.

Introducing Feynman parameters, see (A.1), the matrix element becomes:

$$\imath\mathcal{M} = (\epsilon_1 \cdot \epsilon_2)\,(\epsilon_3 \cdot \epsilon_4)\,4e^4 \int \frac{d^4p}{(2\pi)^4} \int_0^1 dx \int_0^1 dy\, \frac{\delta\,(x+y-1)}{D^2}\,,$$

where D is

$$\begin{aligned} D :=& x\left[(p+q_1+q_2)^2 - m_\pi^2 + \imath\epsilon\right] + y\left[p^2 - m_\pi^2 + \imath\epsilon\right] \\ =& p^2 - m^2 + \imath\epsilon + x\,(q_1+q_2)^2 + 2xp\,(q_1+q_2)\ . \end{aligned}$$

To complete the square, p is substituted by

$$l = p - x\,(q_1+q_2)\ ,$$

which gives

$$D = l^2 - m^2 + \imath\epsilon + (x-x^2)\,(q_1+q_2)^2 =: l^2 - \Delta\,.$$

Then

$$\imath\mathcal{M} = (\epsilon_1 \cdot \epsilon_2)\,(\epsilon_3 \cdot \epsilon_4)\,4e^4 \int_0^1 dx \int_0^1 dy \int \frac{d^4l}{(2\pi)^4} \frac{\delta\,(x+y-1)}{\left(l^2-\Delta\right)^2}\,. \tag{7.5}$$

The benefit of the Feynman parametrization is that the integrand of the four-vector integration is now even and, after Wick-rotation, can be evaluated in spherical coordinates by integrating over the radius and over the solid angle. Since the integrand is not dependent on the angle, the last integration is trivial. The integral over the radius is divergent. To handle the divergence, the dimensional regularization in $d = 4 - 2\epsilon$ dimensions, where ϵ is assumed to be small, is applied. This procedure leads to the formula from section A.1

$$\begin{aligned} \int \frac{d^dl}{(2\pi)^d} \frac{1}{\left(l^2-\Delta\right)^2} =& \frac{\imath}{(4\pi)^{2-\epsilon}} \frac{\Gamma(\epsilon)}{\Gamma(2)} \left(\frac{1}{\Delta}\right)^\epsilon \\ =& \frac{\imath}{(4\pi)^2} \left(\frac{1}{\epsilon} - \gamma_E + \ln(4\pi) - \ln(\Delta)\right)\,, \end{aligned}$$

which will be applied to compute Eq. (7.5).

To compare with the result from the optical theorem, only the imaginary part in the forward region of the matrix element is needed:

$$\begin{aligned}\operatorname{Im}\mathcal{M} &= (\epsilon_1\cdot\epsilon_2)\,(\epsilon_3\cdot\epsilon_4)\,4e^4\operatorname{Im}\int\limits_0^1 dx\,\frac{1}{(4\pi)^2}\left(\frac{1}{\epsilon}-\gamma_E+\ln(4\pi)-\ln(\Delta)\right)\\ &= (\epsilon_1\cdot\epsilon_2)\,(\epsilon_3\cdot\epsilon_4)\,\frac{\beta e^4}{8\pi}\cdot 2\,.\end{aligned}$$

This is, as expected, the same equation as (7.1) from the calculation using the optical theorem and so verifies the previous result.

7.2.2 Triangle Diagram

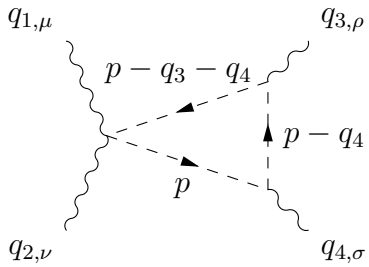

Figure 7.5: Triangle diagram for light-by-light scattering with a charged pion loop.

The matrix element for the triangle diagram shown in Fig. 7.5 is:

$$\begin{aligned}\imath\mathcal{M} = &\int\frac{d^4p}{(2\pi)^4}\epsilon_{1,\mu}\epsilon_{2,\nu}\;2\imath e^2 g^{\mu\nu}\;\times\\ &\frac{\imath\;\imath\;\imath\;\left[(-\imath e)(p+(p+q_4))^\sigma\;\right]\left[(-\imath e)((p-q_4)+(p-q_3-q_4))^\rho\;\right]}{\left[p^2-m^2+\imath\epsilon\right]\;\left[(p-q_4)^2-m^2+\imath\epsilon\right]\;\left[(p-q_3-q_4)^2-m^2+\imath\epsilon\right]}\epsilon_{4,\sigma}\;\epsilon_{3,\rho}\,.\end{aligned}$$

Introducing Feynman parameters, one gets

$$\imath\mathcal{M} = (\epsilon_1\cdot\epsilon_2)\,\epsilon_{3,\rho}\epsilon_{4,\sigma}(-4e^4)\int\limits_0^1 dx\int\limits_0^1 dy\int\limits_0^1 dz\;\int\frac{d^4p}{(2\pi)^4}\frac{N}{D^3}\,\delta\left(x+y+z-1\right)\,,$$

with

$$\begin{aligned}N =&(2p+q_4)^\sigma\,(2p-q_3-2q_4)^\rho\\ D =&p^2-m^2+\imath\epsilon-2p\,(yq_4+z\,(q_3+q_4))+yq_4^2+z\,(q_3+q_4)^2\;.\end{aligned}$$

After substitution with

$$l = p-(yq_4+z\,(q_3+q_4))\;,$$

N and D become

$$\begin{aligned} N =& 4l^\sigma l^\rho + ((1+2y)q_4 + 2z\,(q_3+q_4))^\sigma\,((-1+2y)q_4 + (-1+2z)(q_3+q_4))^\rho, \\ D =& l^2 \underbrace{-m^2 + \imath\epsilon + (y-y^2)q_4^2 + (z-z^2)\,(q_3+q_4)^2 - 2yzq_4\,(q_3+q_4)}_{=:-\Delta}\,. \end{aligned}$$

Integrating the matrix element in l yields:

$$\begin{aligned} \imath\mathcal{M} =& \epsilon_{1,\mu}\epsilon_{2,\nu}\epsilon_{3,\rho}\epsilon_{4,\sigma}(-4e^4)\int_0^1 dy \int_0^{1-y} dz\,\frac{\imath}{(4\pi)^2}\cdot \\ & \left[\imath g^{\rho\sigma}\left(\frac{1}{\epsilon} - \gamma_E + \ln(4\pi) - \ln(\Delta)\right)\right. \\ & \left. - \frac{((1+2y)q_4 + 2z\,(q_3+q_4))^\sigma\,((-1+2y)q_4 + (-1+2z)(q_3+q_4))^\rho}{2\Delta}\right]. \end{aligned} \tag{7.6}$$

For real photons the last line in (7.6), which contains 2Δ in the denominator, vanishes when multiplied by $\epsilon_{3,\rho}\epsilon_{4,\sigma}$. To show this one can make use of the fact that $\epsilon^0 = 0$ and $\vec{q}_3 = -\vec{q}_4$:

$$0 = \epsilon_{3,\rho}q_3^\rho = \vec{\epsilon}_3\vec{q}_3 = \vec{\epsilon}_3(-\vec{q}_3) = \vec{\epsilon}_3\vec{q}_4 = \epsilon_{3,\rho}q_4^\rho\,.$$

Analogue

$$0 = \epsilon_{4,\sigma}q_4^\sigma = \epsilon_{4,\sigma}q_3^\sigma\,,$$

so the numerator becomes zero, and the final result after integrating the two Feynman integrals becomes:

$$\operatorname{Im}\mathcal{M} = (\epsilon_1\cdot\epsilon_2)\,\epsilon_{3,\rho}\epsilon_{4,\sigma}\left[g^{\rho\sigma}\frac{\beta e^4}{8\pi}\left(-1 + \frac{1-\beta^2}{2\beta}\ln\left(\frac{1+\beta}{1-\beta}\right)\right)\right].$$

This verifies the result (7.2) from the optical theorem.

7.2.3 Box Diagram

There are two kinds of box diagrams, shown in Fig. 7.6 and 7.7, which contribute differently to the matrix element.

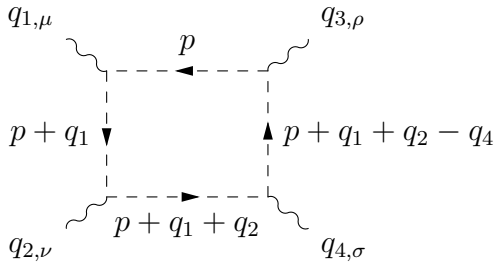

Figure 7.6: Box diagram for light-by-light scattering with a charged pion loop.

The matrix element $\mathcal{M}_1$ for the first box diagram, Fig. 7.6, is:

$$\begin{aligned}
\imath\mathcal{M}_1 = &\int \frac{d^4p}{(2\pi)^4}\epsilon_{1,\mu}\left(-\imath e\right)\left(p+(p+q_1)\right)^\mu \frac{\imath}{(p+q_1)^2-m^2+\imath\epsilon} \\
&\epsilon_{2,\nu}\left(-\imath e\right)\left((p+q_1)+(p+q_1+q_2)\right)^\nu \frac{\imath}{(p+q_1+q_2)^2-m^2+\imath\epsilon} \\
&\epsilon_{4,\sigma}\left(-\imath e\right)\left((p+q_1+q_2)+(p+q_1+q_2-q_4)\right)^\sigma \frac{\imath}{(p+q_1+q_2-q_4)^2-m^2+\imath\epsilon} \\
&\epsilon_{3,\rho}\left(-\imath e\right)\left((p+q_1+q_2-q_4)+p\right)^\rho \frac{\imath}{p^2-m^2+\imath\epsilon} \\
=&\epsilon_{1,\mu}\epsilon_{2,\nu}\epsilon_{3,\rho}\epsilon_{4,\sigma}e^4\int_0^1 dx\int_0^1 dy\int_0^1 dz\int_0^1 dw\int\frac{d^4p}{(2\pi)^4}\frac{6N}{D^4}\delta\left(x+y+z+w-1\right),
\end{aligned} \tag{7.7}$$

with

$$\begin{aligned}
N =&(2p+q_1)^\mu\left(2p+2q_1+q_2\right)^\nu\left(2p+q_1+q_2-q_4\right)^\rho\left(2p+2q_1+2q_2-q_4\right)^\sigma, \\
D =&p^2-m^2+\imath\epsilon+2p\left(xq_1+y(q_1+q_2)+z(q_1+q_2-q_4)\right) \\
&+xq_1^2+y\left(q_1+q_2\right)^2+z\left(q_1+q_2-q_4\right)^2.
\end{aligned}$$

Shifting p by the following l in (7.7),

$$l = p+\left(xq_1+y(q_1+q_2)+z(q_1+q_2-q_4)\right),$$

gives

$$
\begin{aligned}
N =& 16 l^\mu l^\nu l^\rho l^\sigma \\
&+ 4 l^\mu l^\nu \quad (\quad -2xq_1 - \quad 2y(q_1+q_2) + \quad (1-2z)(q_1+q_2-q_4))^\rho \\
&\qquad\quad (\quad -2xq_1 + \quad (1-2y)(q_1+q_2) + \quad (1-2z)(q_1+q_2-q_4))^\sigma \\
&+ 4 l^\mu l^\rho \quad (\quad (1-2x)q_1 + \quad (1-2y)(q_1+q_2) - \quad 2z(q_1+q_2-q_4))^\nu \\
&\qquad\quad (\quad -2xq_1 + \quad (1-2y)(q_1+q_2) + \quad (1-2z)(q_1+q_2-q_4))^\sigma \\
&+ 4 l^\mu l^\sigma \quad (\quad (1-2x)q_1 + \quad (1-2y)(q_1+q_2) - \quad 2z(q_1+q_2-q_4))^\nu \\
&\qquad\quad (\quad -2xq_1 - \quad 2y(q_1+q_2) + \quad (1-2z)(q_1+q_2-q_4))^\rho \\
&+ 4 l^\nu l^\rho \quad (\quad (1-2x)q_1 - \quad 2y(q_1+q_2) - \quad 2z(q_1+q_2-q_4))^\mu \\
&\qquad\quad (\quad -2xq_1 + \quad (1-2y)(q_1+q_2) + \quad (1-2z)(q_1+q_2-q_4))^\sigma \\
&+ 4 l^\nu l^\sigma \quad (\quad (1-2x)q_1 - \quad 2y(q_1+q_2) - \quad 2z(q_1+q_2-q_4))^\mu \\
&\qquad\quad (\quad -2xq_1 - \quad 2y(q_1+q_2) + \quad (1-2z)(q_1+q_2-q_4))^\rho \\
&+ 4 l^\rho l^\sigma \quad (\quad (1-2x)q_1 - \quad 2y(q_1+q_2) - \quad 2z(q_1+q_2-q_4))^\mu \\
&\qquad\quad (\quad (1-2x)q_1 + \quad (1-2y)(q_1+q_2) - \quad 2z(q_1+q_2-q_4))^\nu \\
&+ \qquad (\quad (1-2x)q_1 - \quad 2y(q_1+q_2) - \quad 2z(q_1+q_2-q_4))^\mu \\
&\qquad\quad (\quad (1-2x)q_1 + \quad (1-2y)(q_1+q_2) - \quad 2z(q_1+q_2-q_4))^\nu \\
&\qquad\quad (\quad -2xq_1 - \quad 2y(q_1+q_2) + \quad (1-2z)(q_1+q_2-q_4))^\rho \\
&\qquad\quad (\quad -2xq_1 + \quad (1-2y)(q_1+q_2) + \quad (1-2z)(q_1+q_2-q_4))^\sigma \,, \qquad (7.8)
\end{aligned}
$$

and

$$
\begin{aligned}
D =& l^2 - m^2 + \imath\epsilon + \left(x - x^2\right) q_1^2 + \left(y - y^2\right) (q_1+q_2)^2 + \left(z - z^2\right) (q_1+q_2-q_4)^2 \\
&- 2xyq_1 (q_1+q_2) - 2xzq_1 (q_1+q_2-q_4) - 2yz (q_1+q_2)(q_1+q_2-q_4) \\
=:& l^2 - \Delta + \imath\epsilon \,.
\end{aligned}
$$

For real photons, (7.8) simplifies to:

$$
\begin{aligned}
N =& 16 l^\mu l^\nu l^\rho l^\sigma \\
&+ 16 (x^2 \, l^\mu l^\nu q_1^\rho q_1^\sigma + xz (l^\mu l^\rho q_3^\nu q_1^\sigma + l^\mu l^\sigma q_3^\nu q_1^\rho + l^\nu l^\rho q_3^\mu q_1^\sigma + l^\nu l^\sigma q_3^\mu q_1^\rho) + z^2 l^\rho l^\sigma q_3^\mu q_3^\nu) \\
&+ 16 x^2 z^2 \, q_3^\mu q_3^\nu q_1^\rho q_1^\sigma \,, \\
D =& l^2 - m^2 + y(1-x-y-z)s + xzt + \imath\epsilon \,.
\end{aligned}
$$

The imaginary part of the l-integration gives:

$$\begin{aligned}
&\operatorname{Im}\frac{1}{i}\int\frac{d^{4-2\epsilon}l}{(2\pi)^4}\frac{6N}{(l^2-\Delta+\imath\epsilon)^4}\\
&\quad=-\frac{4}{(4\pi)^2}\left(g^{\mu\nu}g^{\rho\sigma}+g^{\mu\rho}g^{\nu\sigma}+g^{\mu\sigma}g^{\nu\rho}\right)\operatorname{Im}\ln(\Delta-\imath\epsilon)\\
&\qquad-\frac{8}{(4\pi)^2}\left(x^2\,g^{\mu\nu}q_1^\rho q_1^\sigma+z^2 g^{\rho\sigma}q_3^\mu q_3^\nu\right.\\
&\qquad\qquad\left.+xz(g^{\mu\rho}q_3^\nu q_1^\sigma+g^{\mu\sigma}q_3^\nu q_1^\rho+g^{\nu\rho}q_3^\mu q_1^\sigma+g^{\nu\sigma}q_3^\mu q_1^\rho)\right)\operatorname{Im}\frac{1}{\Delta-\imath\epsilon}\\
&\qquad+\frac{16}{(4\pi)^2}x^2z^2\,q_3^\mu q_3^\nu q_1^\rho q_1^\sigma\operatorname{Im}\frac{1}{(\Delta-\imath\epsilon)^2}\,.
\end{aligned}\tag{7.9}$$

In the forward scattering region, the product of the four-momenta of the real photons and epsilon tensors is always zero. The matrix element then becomes

$$\begin{aligned}
\operatorname{Im}\mathcal{M}_1=&-\frac{e^4}{2\pi^2}\int_0^1 dx\int_0^{1-x}dz\int_0^{1-x-z}dy\,\operatorname{Im}\ln(\Delta-\imath\epsilon)\\
=&\frac{e^4}{2\pi}\int_0^1 dx\int_0^{1-x}dz\int_0^{1-x-z}dy\,\Theta\left(y(1-x-y-z)-\frac{1-\beta^2}{4}\right)\,.
\end{aligned}$$

For $y=0$, the Heaviside theta θ is zero and the zero-poles of its argument are

$$\begin{aligned}
&y_\pm(1-x-y_\pm-z)-\frac{1-\beta^2}{4}=0\\
\Rightarrow&y_\pm=\frac{1-x-z\pm\sqrt{(1-x-z)^2-(1-\beta^2)}}{2}\,,
\end{aligned}$$

so the Heaviside theta is 1 when y is between y_- and y_+, which also implies that the discriminant must not be negative, which means that $z\leq 1-x-\sqrt{1-\beta^2}$ and $x\leq 1-\sqrt{1-\beta^2}$. Using this information, the integrals can be rewritten as:

$$\begin{aligned}
\operatorname{Im}\mathcal{M}_1=&\frac{e^4}{2\pi}\int_0^{1-\sqrt{1-\beta^2}}dx\int_0^{1-x-\sqrt{1-x-\beta^2}}dz\int_{y_-}^{y_+}dy\\
=&\frac{e^4}{2\pi}\int_0^{1-\sqrt{1-\beta^2}}dx\int_0^{1-x-\sqrt{1-x-\beta^2}}dz\;\sqrt{(1-x-z)^2-(1-\beta^2)}\,.
\end{aligned}$$

Now substituting $\xi=1-x$ and $\zeta=\xi-z$ and then using the integration table

from [14]:

$$\begin{aligned}
\operatorname{Im}\mathcal{M}_1 =& \frac{e^4}{2\pi} \int_1^{\sqrt{1-\beta^2}} d\xi \int_\xi^{\sqrt{\xi-\beta^2}} d\zeta \sqrt{\zeta^2-(1-\beta^2)} \\
=& \frac{e^4}{4\pi} \int_1^{\sqrt{1-\beta^2}} d\xi \left(-\xi\sqrt{\xi^2-(1-\beta^2)} + (1-\beta^2)\operatorname{arcosh}(\frac{\xi}{\sqrt{1-\beta^2}}) \right) \\
=& \frac{e^4}{2\pi} \left(-\frac{\beta^3}{3} + \frac{\beta}{2} - \frac{1-\beta^2}{4} \ln\left(\frac{1+\beta}{1-\beta}\right) \right) .
\end{aligned}$$

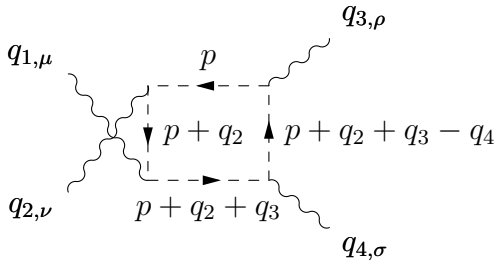

Figure 7.7: Box diagram for light-by-light scattering with a charged pion loop with crossed incoming photon lines.

The box with crossed incoming photon lines (Fig. 7.7) is related with Fig. 7.6 by $t \leftrightarrow u$ symmetry. That simplifies the calculation. One can start at Eq. (7.9), which then leads in the same way as above to the imaginary part of the forward scattering matrix element $\mathcal{M}_2$ for the crossed box:

$$\operatorname{Im}\mathcal{M}_2 = -\frac{e^4}{2\pi^2} \int_0^1 dx \int_0^{1-x} dz \int_0^{1-x-z} dy \operatorname{Im}\ln(\Delta' - \imath\epsilon) ,$$

where Δ' is related to Δ by substituting t by u. Because of

$$\left. \begin{array}{c} s+t+u = \sum_{i=1}^4 q_i^2 = 0 \\ t = 0 \end{array} \right\} \Rightarrow u = -s ,$$

Δ' is

$$\Delta' = m^2 - y(1-x-y-z)s + xzs ,$$

The matrix element is then

$$\begin{aligned}
\operatorname{Im}\mathcal{M}_2 =& \frac{e^4}{2\pi} \int_0^1 dx \int_0^{1-x} dz \int_0^{1-x-z} dy\, \Theta\left(y(1-x-y-z) - xz - \frac{1-\beta^2}{4} \right) \\
=& \frac{e^4}{2\pi} \int_0^{1-\sqrt{1-\beta^2}} dx \int_0^{1+x-\sqrt{4x+1-\beta^2}} dz \sqrt{(1-x-z)^2 - 4xz - (1-\beta^2)} .
\end{aligned}$$

By substituting $\zeta = 1 + x - z$, one gets the result for $\operatorname{Im}\mathcal{M}_2$:

$$\begin{aligned}\operatorname{Im}\mathcal{M}_2 =& -\frac{e^4}{2\pi}\int\limits_0^{1-\sqrt{1-\beta^2}} dx \int\limits_{1+x}^{\sqrt{4x+1-\beta^2}} d\zeta\,\sqrt{\zeta^2-4x-(1-\beta^2)} \\ =& \frac{e^4}{8\pi}\left(-\frac{\beta}{2}+\frac{5\beta^3}{6}-\frac{-\beta^4+2\beta^2+3}{4}\ln\left(\frac{1+\beta}{1-\beta}\right)\right) .\end{aligned}$$

The total result for the box diagrams is

$$\begin{aligned}\operatorname{Im}\mathcal{M} =& 2\mathcal{M}_1 + 2\mathcal{M}_2 \\ =& \frac{\beta e^4}{8\pi}\left(3-\beta^2-\frac{(1-\beta^2)(3+\beta^2)}{2\beta}\ln\left(\frac{1+\beta}{1-\beta}\right)\right) ,\end{aligned}$$

where the factors of two reflect the fact that the diagrams can be drawn overhead, changing $q_1 \leftrightarrow q_2$ and $q_4 \leftrightarrow q_3$ simultaneously, so there are 4 diagrams in total. This result is the same as the one in Eq. (7.3) and now all results calculated by the optical theorem in Sec. 7.1 are confirmed by the direct Feynman diagrams technique.

7.3 Partial Wave Decomposition

Applying the partial wave decomposition of Chapter 4 to the Born diagrams, Eq. (7.4), one gets the following waves $B_{J\Lambda}$ for the total angular momentum J up to 2:

$$\begin{aligned}B_{00} =& \frac{1-\beta^2}{2\beta}\ln\left(\frac{1+\beta}{1-\beta}\right) , \\ B_{20} =& \frac{1-\beta^2}{\beta^2}\frac{\sqrt{5}}{4}\left(-6+\frac{3-\beta^2}{\beta}\ln\left(\frac{1+\beta}{1-\beta}\right)\right) , \\ B_{22} =& \frac{\sqrt{15}}{4\sqrt{2}}\left(\frac{10}{3}-\frac{2}{\beta^2}+\frac{(1-\beta^2)^2}{\beta^3}\ln\left(\frac{1+\beta}{1-\beta}\right)\right) .\end{aligned}$$

As shown in Fig. 7.8, the B_{00} wave is most prominent in the low-energy region and is overtaken by the B_{22} wave at higher energies. The B_{20} wave is always comparatively small. In principle, also higher waves, $J > 2$, exist. Their influence will be discussed in more detail in Sec. 7.4.3.

7.4 Hadronic Light-by-Light by the Optical Theorem for Virtual Photons

The calculations so far are only valid for real photons and will now be generalized to virtual photons.

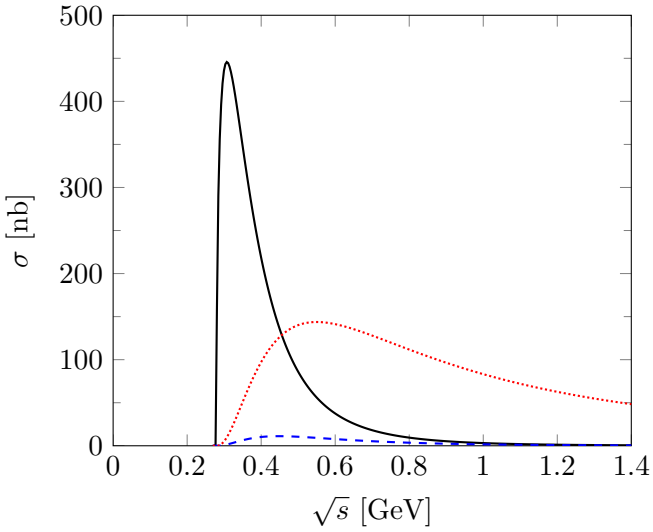

Figure 7.8: Integrated $\gamma\gamma \to \pi\pi$ cross section for the the B_{00} wave (solid-black line), B_{22} wave (dotted-red line) and B_{20} wave (dashed-blue line).

7.4.1 Kinematics

For convenience, the virtualities of the photons Q_i, where $i = 1 \ldots 4$, the crossing-symmetric variable ν and the virtual photon flux factor X are defined as follows:

$$\begin{aligned} Q_i^2 :=& -q_i^2 \,, \\ \nu :=& q_1 \cdot q_2 = \frac{1}{2}(s + Q_1^2 + Q_2^2) \,, \\ X :=& \nu^2 - Q_1^2 Q_2^2 \,. \end{aligned}$$

In the center of mass frame as choosen in Fig. 7.2 the relations between the kinematic variables are the following:

$$\begin{aligned} E_{\pi_1} =& E_{\pi_2} = \frac{\sqrt{s}}{2} \,, \\ |\vec{p}_{1,2}| =& \frac{\sqrt{s}}{2}\beta \,, \end{aligned}$$

$$
\begin{aligned}
Q_1^2 &= -(q_1^0)^2 + |\vec{q}_1|^2 \,, \\
Q_2^2 &= -(q_2^0)^2 + |\vec{q}_2|^2 = -(\sqrt{s} - q_1^0)^2 + |\vec{q}_1|^2 \,, \\
\Rightarrow Q_1^2 - Q_2^2 &= s - 2\sqrt{s} q_1^0 \,, \\
\Rightarrow q_1^0 &= \frac{s - Q_1^2 + Q_2^2}{2\sqrt{s}} = \frac{\nu - Q_1^2}{\sqrt{s}} \,, \\
q_2^0 &= \frac{s + Q_1^2 - Q_2^2}{2\sqrt{s}} = \frac{\nu - Q_2^2}{\sqrt{s}} \,, \\
|\vec{q}_1| &= |\vec{q}_2| = \sqrt{(q_2^0)^2 + Q_2^2} = \sqrt{\frac{X}{s}} \,.
\end{aligned}
$$

7.4.2 Form Factors

Up to now, the calculation carried out considered only point-like interactions between γ and π. For a virtual photon one becomes sensitive to the internal structure of the interaction, which is expressed through the dependence on the virtuality. This requires the introduction of form factors $F(Q_i^2, p^2)$ in the $\gamma\pi\pi$ and the $\gamma\gamma\pi\pi$ vertex, where Q_i^2 is the virtuality of the photon and p^2 the mass of the off-shell pion. The other pion is on-shell.

With the abbreviations

$$
\begin{aligned}
F(Q_i^2, p^2) &=: F_i^{p^2} \,, \text{ for } i = 1, 2 \,, \\
F(Q_1^2, Q_2^2, s, t) &=: F_{1,2}^G \,,
\end{aligned}
$$

the introduction of the form factors can be visualized by

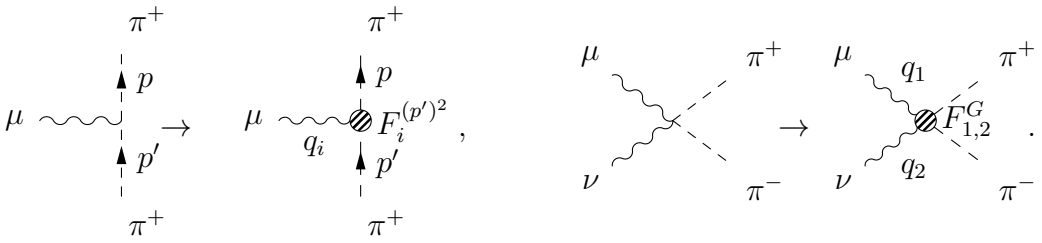

The corresponding Born diagrams are shown in Fig. 7.9. The form factors are constrained by the following conditions:

1. Gauge invariance of the sum of the diagrams must be retained.

2. In the limit where the photons are real the point-like interaction must be restored which means $F \to 1$.

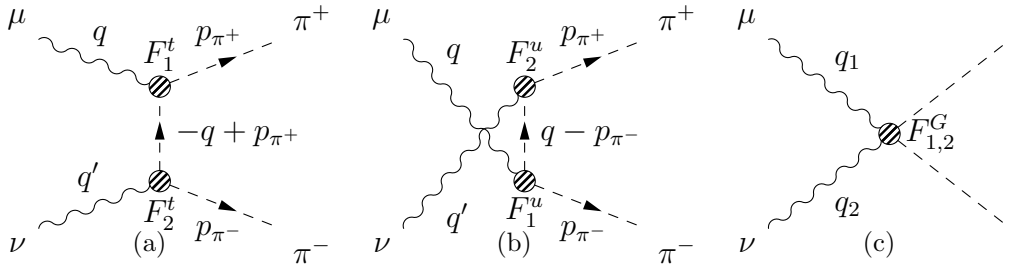

Figure 7.9: Born diagrams for $\gamma^*\gamma^* \to \pi^+\pi^-$ with form factors

The matrix element for the sum of the three diagrams in Fig. 7.9 is

$$\begin{aligned} M =& \epsilon_{1,\mu}\epsilon_{2,\nu}M^{\mu\nu}\,, \\ \epsilon_i \equiv& \epsilon(q_i,\lambda_i)\,, \\ M^{\mu\nu} =& -e^2(2p_1-q_1)^\mu F_1^t \frac{1}{(p_1-q_1)^2-m_\pi^2}(-2p_2+q_2)^\nu F_2^t \\ & -e^2(-2p_2+q_1)^\mu F_1^u \frac{1}{(-p_2+q_1)^2-m_\pi^2}(2p_1-q_2)^\nu F_2^u \\ & +2e^2 F_{1,2}^G g^{\mu\nu}\,. \end{aligned} \tag{7.10}$$

The gauge invariance can be forced by requiring the ward identities:

$$\begin{aligned} \epsilon_{1\mu}q_{2\nu}M^{\mu\nu} &= 0\,, \\ \epsilon_{2\nu}q_{1\mu}M^{\mu\nu} &= 0\,, \end{aligned}$$

which expand to

$$\begin{aligned} 0 \stackrel{!}{=}& \epsilon_{1\mu}q_{2\nu}M^{\mu\nu} \\ =& e^2F_1^tF_2^t\frac{-Q_2^2-2q_2\cdot p_2}{Q_1^2+2p_1\cdot q_1}(2\epsilon_1\cdot p_1) \\ & + e^2F_1^uF_2^u\frac{Q_2^2+2q_2\cdot p_1}{Q_1^2+2p_2\cdot q_1}(-2\epsilon_1\cdot p_2) \\ & + 2e^2F_{1,2}^G\epsilon_1\cdot q_2 \\ =& -2e^2\left(F_1^tF_2^t\epsilon_1\cdot p_1 + F_1^uF_2^u\epsilon_1\cdot p_2 - F_{1,2}^G\epsilon_1\cdot q_2\right)\,, \end{aligned} \tag{7.11}$$

where in the last step

$$\begin{aligned} Q_2^2+2q_2\cdot p_2 &= -(q_2-p_2)^2+m_\pi^2 = -(q_1-p_1)^2+m_\pi^2 = Q_1^2+2p_1\cdot q_1\,, \\ Q_2^2+2q_2\cdot p_1 &= Q_1^2+2p_2\cdot q_1\,, \end{aligned}$$

were used. Similarly

$$\begin{aligned} 0 \stackrel{!}{=}& \epsilon_{2\nu}q_{1\mu}M^{\mu\nu} \\ =& -2e^2\left(F_1^tF_2^t\epsilon_2\cdot p_2 + F_1^uF_2^u\epsilon_2\cdot p_1 - F_{1,2}^G\epsilon_2\cdot q_1\right)\,. \end{aligned}$$

The form factors do neither depend on the helicities nor on the frame. So when choosing the c. m. and a transversal photon, $\epsilon_1^0 \equiv 0$, then $\epsilon_1 \cdot q_2 = 0$ because $\epsilon_1 \cdot q_1 = 0$, so (7.11) simplifies to

$$\begin{aligned} 0 =& F_1^t F_2^t \epsilon_1 \cdot p_1 + F_1^u F_2^u \epsilon_1 \cdot p_2 \\ =& (F_1^t F_2^t - F_1^u F_2^u) \epsilon_1 \cdot p_1 \,. \end{aligned}$$

This expression can be further simplified. One can choose the coordinate system in a way that the photons travel along the z-axis and the pion p_1 travels in the x-z-plane. The polarization of the photon q_1 can be choosen so that $\epsilon = (0, -1/\sqrt{2}, -i/\sqrt{2}, 0)$. Then $\epsilon_1 \cdot p_1 = -p_1^1/\sqrt{2}$ which is in general not equal to zero, so the other factor in the previous equation has to be zero:

$$0 = F_1^t F_2^t - F_1^u F_2^u \,.$$

One can now make use of the second condition: If the second photon is real then $F_2^{t,u} = 1$ and consequently $0 = F_1^t - F_1^u$. This means that $F_i^{p^2}$ cannot depend on p^2:

$$F(Q_i^2, p^2) \equiv F(Q_i^2) =: F_i \,, \text{ for } i = 1, 2 \,. \tag{7.12}$$

This constraint is imposed by only considering a pion running between the two photon vertices. In a more general case, one would also have to consider excited states like vector-mesons and the form factors would then be dependend on p^2 (see, for example Ref. [19] where this point is discussed).

Using (7.12) the equation (7.11) becomes

$$0 = F_1 F_2 \epsilon_1 \cdot (\underbrace{p_1 + p_2}_{q_1 + q_2}) - F_{1,2}^G \epsilon_1 \cdot q_2 = (F_1 F_2 - F_{1,2}^G) \epsilon_1 \cdot q_2 \,.$$

$\epsilon_1 \cdot q_2$ is in general not zero, which one can see when the photons have different virtualities Q_1^2 and Q_2^2 and are longitudinal polarized

$$\epsilon_i = \sqrt{Q_i^{-2}} (|\vec{q}_i|, 0, 0, q_i^0) \,.$$

This means:

$$F_{1,2}^G \equiv F_1 F_2 \,.$$

A very simple choice for the form factors F_1 and F_2 is to invoke the Vector Meson Dominance (VMD). The VMD parametrization is based on the assumption that a virtual photon can quantum-mechanically be mixed with a resonance particle that has the same quantum numbers. This particle is a ρ meson. Then, the VMD reads:

$$F_i(Q_i^2) = \frac{m_\rho^2}{m_\rho^2 + Q_i^2} \,, \text{ for } i = 1, 2 \,. \tag{7.13}$$

The shape of this VMD is shown in Fig. 7.10 as well as its doubly virtual counter part.

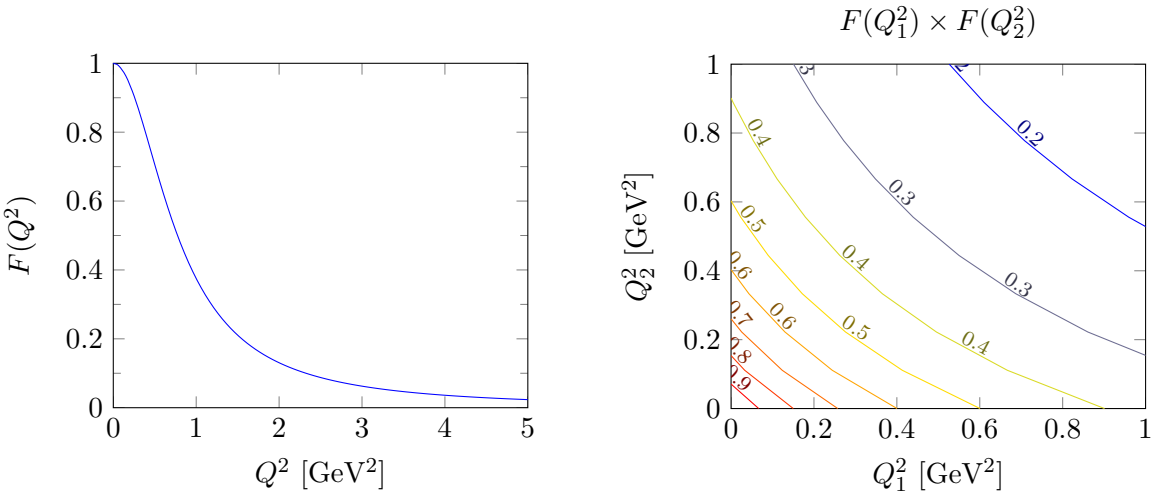

Figure 7.10: Q^2 dependence of the form factor $F(Q^2)$ as given in (7.13) (left) and dependence on Q_1^2 and Q_2^2 of the form factor product $F(Q_1^2)F(Q_2^2)$ (right).

7.4.3 Hadronic Light-by-Light by the Optical Theorem

Analogous to section 7.1 the optical theorem is applied here to virtual photons in the Born approximation, as shown in Fig. 7.9. The matrix element (7.10) is therefore decomposed in the three parts $\mathcal{M}_a, \mathcal{M}_b, \mathcal{M}_c$ which correspond to the diagrams in Fig. 7.9:

$$\begin{aligned}
\mathcal{M}_a &= -4F_1F_2e^2\frac{\epsilon_1\cdot p_1\ \epsilon_2\cdot p_2}{2q_1\cdot p_1+Q_1^2}\,,\\
\mathcal{M}_b &= -4F_1F_2e^2\frac{\epsilon_1\cdot p_2\ \epsilon_2\cdot p_1}{2q_1\cdot p_2+Q_1^2}\,,\\
\mathcal{M}_c &= \quad 2F_1F_2e^2\epsilon_1\cdot\epsilon_2\,.
\end{aligned}$$

The products of the ϵ-tensors with the four-momenta can be evaluated in the center of mass frame shown in Fig. 7.2 and can be rewritten, then, with Lorentz invariants and the scattering angle θ. The final expressions are given in Tab. 7.1. The same is done to the following four-vector products:

$$\begin{aligned}
q_1\cdot p_1 &= q_1^0p_1^0 - |\vec{q}_1||\vec{p}_1|\cos\theta\\
&= \frac{1}{4}(s-Q_1^2+Q_2^2) - \frac{\sqrt{X}}{2}\beta\cos\theta\,,\\
q_1\cdot p_2 &= \frac{1}{4}(s-Q_1^2+Q_2^2) + \frac{\sqrt{X}}{2}\beta\cos\theta\,,\\
\epsilon_1\cdot\epsilon_2 &= \begin{cases} 1 & \text{for } \Lambda=0,\ \lambda_i=\pm1\\ 0 & \text{for } \Lambda=2,\ \lambda_i=\pm1\\ -\frac{\nu}{\sqrt{Q_1^2Q_2^2}} & \text{for } \Lambda=0,\ \lambda_i=0 \end{cases}.
\end{aligned}$$

$\cdot$	q_1	q_2	p_1	p_2
$\epsilon_1^{\lambda=\ 1}$	0	0	$-\frac{\sqrt{s}}{2\sqrt{2}}\beta\sin\theta$	$\frac{\sqrt{s}}{2\sqrt{2}}\beta\sin\theta$
$\epsilon_1^{\lambda=-1}$	0	0	$\frac{\sqrt{s}}{2\sqrt{2}}\beta\sin\theta$	$-\frac{\sqrt{s}}{2\sqrt{2}}\beta\sin\theta$
$\epsilon_1^{\lambda=\ 0}$	0	$\sqrt{\frac{X}{Q_1^2}}$	$\frac{\sqrt{X}-(\nu-Q_1^2)\beta\cos\theta}{2\sqrt{Q_1^2}}$	$\frac{\sqrt{X}+(\nu-Q_1^2)\beta\cos\theta}{2\sqrt{Q_1^2}}$
$\epsilon_2^{\lambda=\ 1}$	0	0	$\frac{\sqrt{s}}{2\sqrt{2}}\beta\sin\theta$	$-\frac{\sqrt{s}}{2\sqrt{2}}\beta\sin\theta$
$\epsilon_2^{\lambda=-1}$	0	0	$-\frac{\sqrt{s}}{2\sqrt{2}}\beta\sin\theta$	$\frac{\sqrt{s}}{2\sqrt{2}}\beta\sin\theta$
$\epsilon_2^{\lambda=\ 0}$	$\sqrt{\frac{X}{Q_2^2}}$	0	$\frac{-\sqrt{X}-(\nu-Q_2^2)\beta\cos\theta}{2\sqrt{Q_2^2}}$	$\frac{-\sqrt{X}+(\nu-Q_2^2)\beta\cos\theta}{2\sqrt{Q_2^2}}$

Table 7.1: Products of the ϵ-tensors with the four-momentum vectors for given helicities.

With the notation and intermediate steps already prepared, one proceeds with the final calculation. Since virtual photons have 3 degrees of freedom, there are several amplitudes $\mathcal{M}_{\lambda_1\lambda_2}$, but after considering parity and time-reversal discrete symmetries, the needed amplitudes are:

$$
\begin{aligned}
\mathcal{M}_{+-} =& -F_1F_2e^2\left(-\frac{\frac{s}{2}\beta^2\sin^2\theta}{\frac{1}{2}(s+Q_1^2+Q_2^2)-\sqrt{X}\beta\cos\theta}-\frac{\frac{s}{2}\beta^2\sin^2\theta}{\frac{1}{2}(s+Q_1^2+Q_2^2)+\sqrt{X}\beta\cos\theta}\right)\\
=&F_1F_2e^2s\beta^2\nu\frac{\sin^2\theta}{\nu^2-X\beta^2\cos^2\theta}\,,\\
\mathcal{M}_{++} =&F_1F_2e^2\left(2-s\beta^2\nu\frac{\sin^2\theta}{\nu^2-X\beta^2\cos^2\theta}\right)\,,\\
\mathcal{M}_{00} =&F_1F_2e^2\frac{1}{\sqrt{Q_1^2Q_2^2}}\Big[-2\nu\\
&-\frac{\Big(\sqrt{X}-(\nu-Q_1^2)\beta\cos\theta\Big)\Big(-\sqrt{X}+(\nu-Q_2^2)\beta\cos\theta\Big)}{\nu-\sqrt{X}\beta\cos\theta}\\
&-\frac{\Big(\sqrt{X}+(\nu-Q_1^2)\beta\cos\theta\Big)\Big(-\sqrt{X}-(\nu-Q_2^2)\beta\cos\theta\Big)}{\nu+\sqrt{X}\beta\cos\theta}\Big]\\
=&2F_1F_2e^2\frac{1}{\sqrt{Q_1^2Q_2^2}}(\nu^2-X\beta^2\cos^2\theta)^{-1}\Big(-\nu^3+X\nu\\
&+\big\{\nu X+(\nu-Q_1^2)(\nu-Q_2^2)\nu-X[\underbrace{(\nu-Q_1^2)+(\nu-Q_2^2)}_{s}]\big\}\beta^2\cos^2\theta\Big)\\
=&2F_1F_2e^2\sqrt{Q_1^2Q_2^2}\,\frac{-\nu+s\beta^2\cos^2\theta}{\nu^2-X\beta^2\cos^2\theta}\,.
\end{aligned}
$$

In the limit of real photons, which means $Q_1^2\to 0$ and $Q_2^2\to 0$, the variable $X\to\nu^2$ and $\nu\to\frac{s}{2}$, the formulas are in perfect agreement with the results from the real photon

calculation, Eq. (7.4), where $\mathcal{M}_{++}$ denotes the $\Lambda = 0$ case and $\mathcal{M}_{+-}$ the $\Lambda = 2$ case. Note that the amplitude $M_{00} \to 0$, as real photons cannot be longitudinally polarized.

The partial wave decomposition $B_{J\Lambda}^{\lambda_1\lambda_2}$ of these matrix elements is:

$$
\begin{aligned}
B_{00}^{++} =& F_1F_2\left(1 - \frac{s\nu}{2X} + \frac{s}{2}\frac{\nu^2-\beta^2X}{\beta X^{3/2}}\operatorname{artanh}(\frac{\beta\sqrt{X}}{\nu})\right),\\
B_{20}^{++} =& F_1F_2\frac{\sqrt{5}}{4}s\left(-3\nu\frac{\nu^2-b^2X}{\beta^2X^2} + \frac{3\nu^4-4\beta^2\nu^2X+\beta^4X^2}{\beta^3X^{5/2}}\operatorname{artanh}(\frac{\beta\sqrt{X}}{\nu})\right),\\
B_{40}^{++} =& -F_1F_2s(\nu^2-\beta^2X)\times\\
&\left(\nu\frac{105\nu^2-55\beta^2X}{16\beta^4X^3} - \frac{105\nu^4-90\beta^2\nu^2X+9\beta^4X^2}{16\beta^5\nu X^{7/2}}\operatorname{artanh}(\frac{\beta\sqrt{X}}{\nu})\right),\\
B_{22}^{+-} =& \frac{F_1F_2}{4}\left(\sqrt{\frac{5}{6}}s\nu\frac{-3\nu^2+5\beta^2X}{\beta^2X^2} + \sqrt{\frac{15}{2}}s\frac{(\nu^2-\beta^2X)^2}{\beta^3X^{5/2}}\operatorname{artanh}(\frac{\beta\sqrt{X}}{\nu})\right),\\
B_{42}^{+-} =& F_1F_2\left(s\nu\frac{-105\nu^4+190\beta^2\nu^2X-81\beta^4X^2}{8\sqrt{10}\beta^4X^3}\right.\\
&\left.+ s\frac{15(\nu^2-\beta^2X)^2(7\nu^2-\beta^2X)}{8\sqrt{10}\beta^5X^{7/2}}\operatorname{artanh}(\frac{\beta\sqrt{X}}{\nu})\right),\\
B_{00}^{00} =& F_1F_2\sqrt{Q_1^2Q_2^2}\left(-\frac{s}{X} + \frac{s\nu-X}{X^{3/2}\beta}\operatorname{artanh}(\frac{\beta\sqrt{X}}{\nu})\right),\\
B_{20}^{00} =& F_1F_2\sqrt{Q_1^2Q_2^2}\frac{\sqrt{5}}{2}(X-s\nu)\left(\frac{3\nu}{X^2\beta^2} + \frac{X\beta^2-3\nu^2}{X(5/2)\beta^3}\operatorname{artanh}(\frac{\beta\sqrt{X}}{\nu})\right).
\end{aligned}
$$

The resulting cross sections of singe partial waves are shown in Fig. 7.11. At low energies, just above the production threshold ($2m_\pi$), the B_{00} wave is dominant, which is then, at about 0.5 GeV, superseded by the B_{22} wave. The B_{20} and the other partial waves have a much smaller amplitude. Note that the B_{00} wave is even more dominant when the photons are virtual.

The differential cross section goes up for high $|\cos\theta|$ at $\sqrt{s} = 0.3\,\text{GeV}$, see Fig. 7.12. This means that even though the B_{00} is by far dominant in this region, the influence of the other partial waves can clearly be seen. For a pure B_{00} wave one would expect the cross section to be independent of the angle θ. The influence of the amount of partial waves selected is illustrated in Fig. 7.13. At the given energy, its contribution is already quite low and does not match well with the Born line. This corresponds to the low amplitude of this wave at that energy, compare Fig. 7.11. One gets much better agreement by also considering the D waves, B_{20} and B_{22}, because they, or more precisely the B_{22} wave, are dominant at $\sqrt{s} = 0.7\,\text{GeV}$. Of course, there is further enhancement when adding higher waves.

The theoretical $\gamma\gamma \to \pi^+\pi^-$ cross section is lower than experimental data at energies around 0.3 GeV and higher than measured data at energies around 0.6 GeV, see

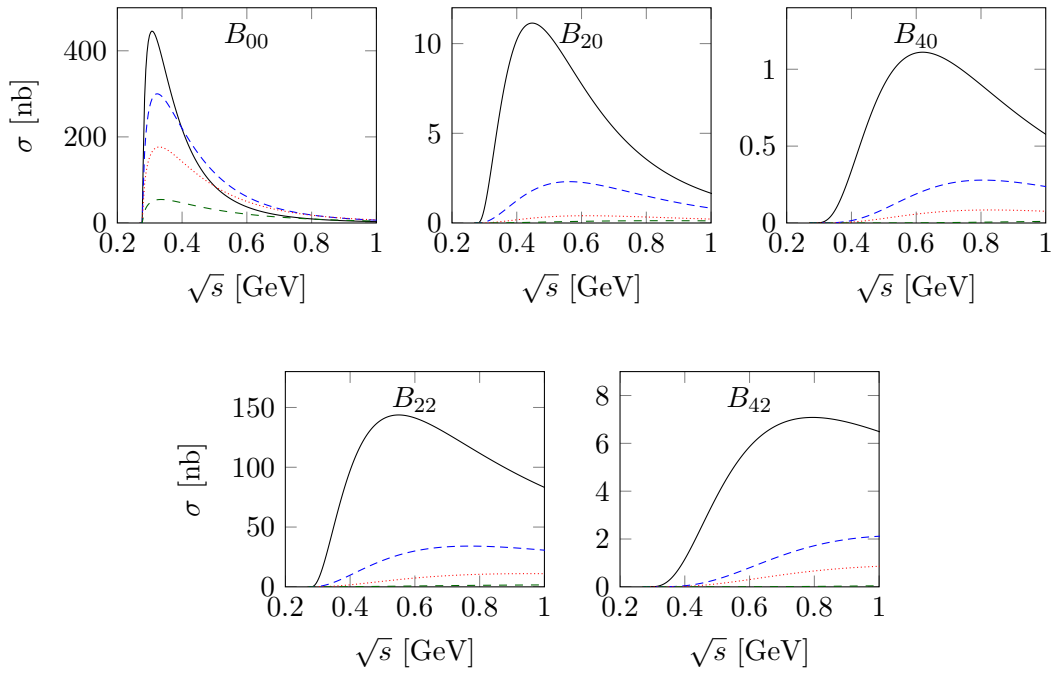

Figure 7.11: $\gamma\gamma \to \pi^+\pi^-$ partial waves (solid-black line), $\gamma^*\gamma^* \to \pi^+\pi^-$ with $Q_1^2 = Q_2^2 = 0.1\,\mathrm{GeV}^2$ (dashed-blue line), $Q_1^2 = Q_2^2 = 0.5\,\mathrm{GeV}^2$ (dashed-green line), and $\gamma^*\gamma \to \pi^+\pi^-$ with $Q^2 = 0.5\,\mathrm{GeV}^2$ (dotted-red line).

Fig. 7.5. This energy region will be improved by unitarization in Sec. 7.5. At higher energies, a $f_2(1270)$ resonance [23] is seen by photons, and since it is not included in the Lagrangian (6.1), that region is not described.

Fig. 7.15 shows that the cross section goes down when the virtualities of the photons go up, but there is a small bump near the production threshold. Note that in case of low virtualities, e. g. $Q_1^2 = Q_2^2 = 0.01\,\mathrm{GeV}^2$, the cross section for virtual photons can be even higher than that of real photons; this is due to the fact that virtual photons can be longitudinally polarized and so there is an additional contribution coming from the $\mathcal{M}^{00}$ matrix element.

The Born diagrams can be split into two parts: First, the form factors, and second, everything else from the diagram. When fixing the form factors to one, $F_1 \equiv F_2 \equiv 1$, one can see, Fig. 7.16, that the bump comes from the second part. This is obvious, because the form factors depend only on the virtualities, not on energy and only scale the whole curve down. The second part enhances the cross section for low energies and decreases it for higher ones. In the high-energy limit (ignoring resonances like the $f_2(1270)$), the virtualities can be neglected, see formulas, which is equal to the fact that all curves in the figure approach one, or, considering form factors, they approach F_1F_2.

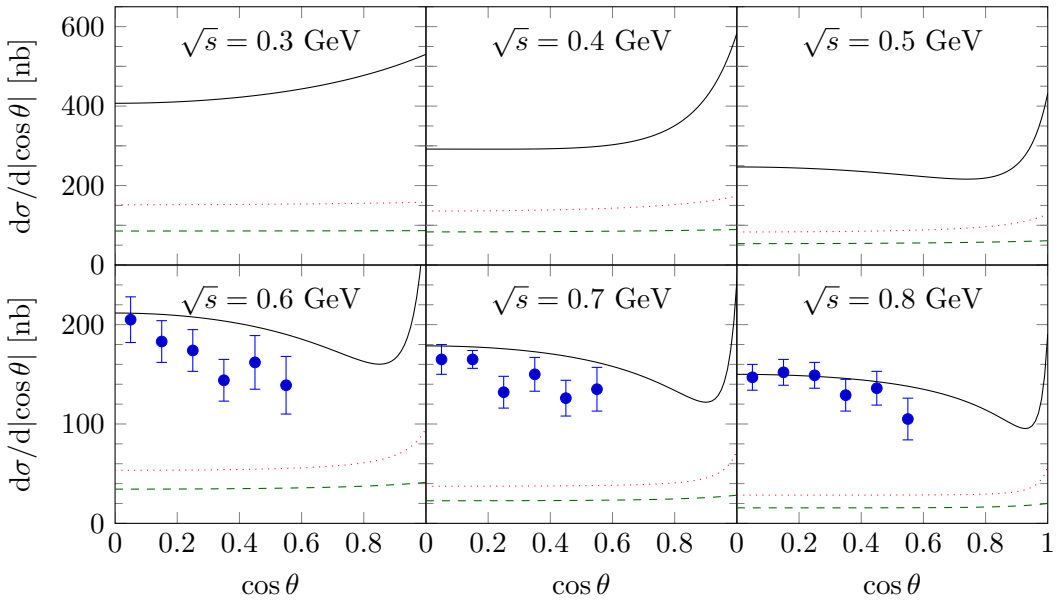

Figure 7.12: $\gamma\gamma \to \pi^+\pi^-$ Born differential cross section (solid-black line), $\gamma^*\gamma \to \pi^+\pi^-$ with $Q^2 = 0.5\,\mathrm{GeV}^2$ (dotted-red line), and $\gamma^*\gamma^* \to \pi^+\pi^-$ with $Q_1^2 = Q_2^2 = 0.5\,\mathrm{GeV}^2$ (dashed-green line). Experimental $\gamma\gamma \to \pi^+\pi^-$ data from Mark II [20] (blue dots).

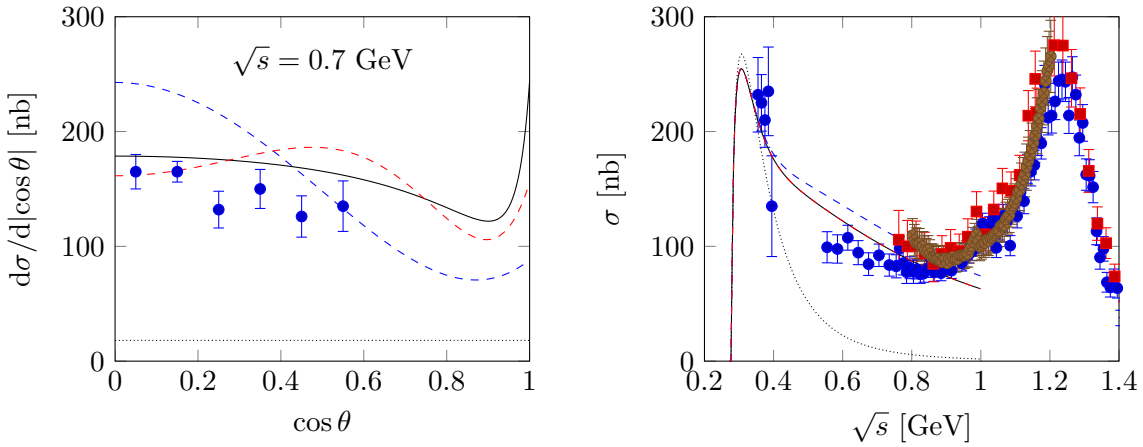

(a) (b)

Figure 7.13: Differential cross section at $\sqrt{s} = 0.7\,\mathrm{GeV}$ (a), and integrated cross section ($|\cos\theta| < 0.6$) (b) for the process $\gamma\gamma \to \pi^+\pi^-$ for the full Born amplitude (solid-black line), S wave (dotted-black line), S and D waves (dashed-blue line), and S, D, and G waves (dashed-red line). Experimental $\gamma\gamma \to \pi^+\pi^-$ data from Mark II [20] (blue dots), Cello [21] (red squares) and Belle [22] (brown dots).

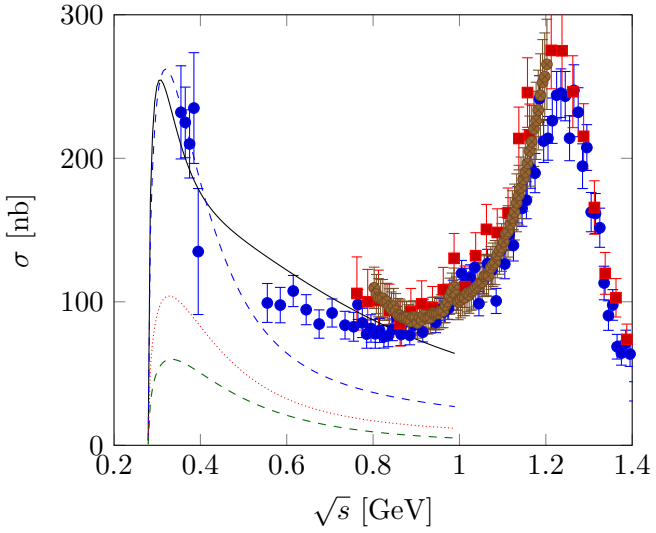

Figure 7.14: $\gamma\gamma \to \pi^+\pi^-$ Born integrated cross section ($|\cos\theta| \leq 0.6$) (solid-black line), $\gamma^*\gamma^* \to \pi^+\pi^-$ with $Q_1^2 = Q_2^2 = 0.1\,\mathrm{GeV}^2$ (dashed-blue line), $Q_1^2 = Q_2^2 = 0.5\,\mathrm{GeV}^2$ (dashed-green line), and $\gamma^*\gamma \to \pi^+\pi^-$ with $Q^2 = 0.5\,\mathrm{GeV}^2$ (dotted-red line). Experimental $\gamma\gamma \to \pi^+\pi^-$ data from Mark II [20] (blue dots), Cello [21] (red squares) and Belle [22] (brown dots).

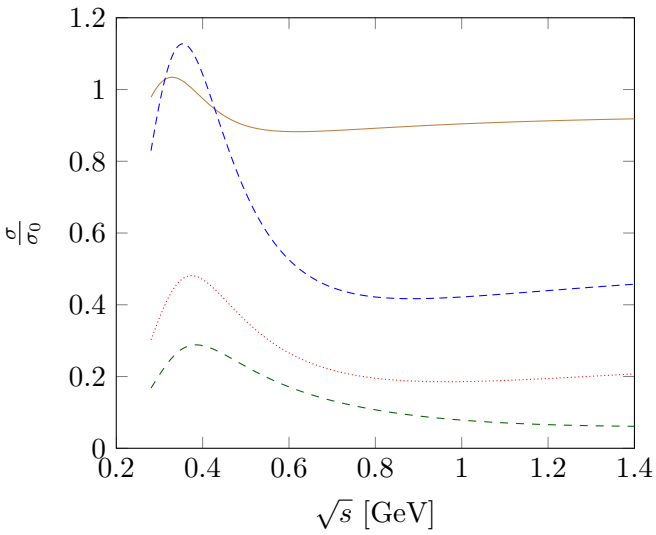

Figure 7.15: $\gamma^*\gamma^* \to \pi^+\pi^-$ Born integrated cross section ($|\cos\theta| \leq 0.6$) with $Q_1^2 = Q_2^2 = 0.01\,\mathrm{GeV}^2$ (solid-brown line), $Q_1^2 = Q_2^2 = 0.1\,\mathrm{GeV}^2$ (dashed-blue line), $Q_1^2 = Q_2^2 = 0.5\,\mathrm{GeV}^2$ (dashed-green line), and $\gamma^*\gamma \to \pi^+\pi^-$ with $Q^2 = 0.5\,\mathrm{GeV}^2$ (dotted-red line), each divided by the real photon cross section.

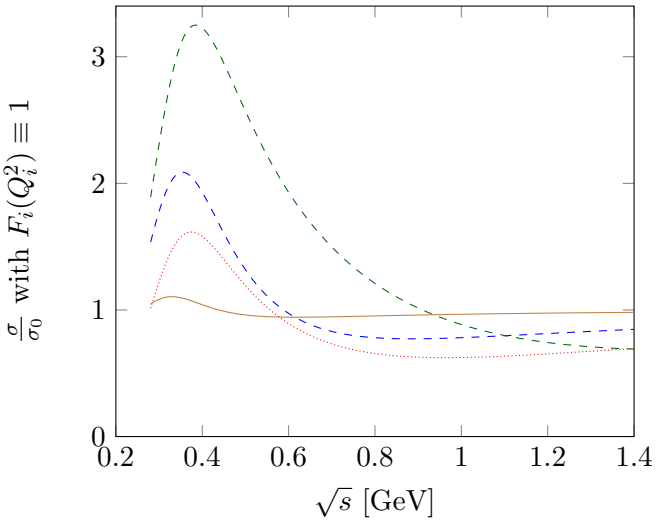

Figure 7.16: $\gamma^*\gamma^* \to \pi^+\pi^-$ Born integrated cross section ($|\cos\theta| \leq 0.6$) with form-factors, $F(Q_i^2) \equiv 1$, $i = 1, 2$, for $Q_1^2 = Q_2^2 = 0.5\,\mathrm{GeV}^2$ (dashed-green line), $Q_1^2 = Q_2^2 = 0.1\,\mathrm{GeV}^2$ (dashed-blue line), $Q_1^2 = Q_2^2 = 0.01\,\mathrm{GeV}^2$ (solid-brown line), and $\gamma^*\gamma \to \pi^+\pi^-$ with $Q^2 = 0.5\,\mathrm{GeV}^2$ (dotted-red line), each divided by the real photon cross section.

7.5 Unitarization of the Partial Wave Amplitude

As seen in the last chapter, the Born amplitudes, although including form factors, have significant deviations from measured data. As it turns out, including final state interactions can improve the description significantly. They are implemented here by unitarization as described in Chapter 5.

7.5.1 Isospin Structure

To be able to unitarize the partial waves, they first have to be decomposed into isospin components. Because the pions couple to a symmetric $\gamma\gamma$ state, only the isospins $I = 0$ and $I = 2$ in the final state are posible. First, the relation between the partial wave for the charged pions $B^C_{J\Lambda}$ is expressed using the isospin components:

$$\begin{aligned}
|\pi^+\pi^-\rangle &= N\{\langle 1\,1, 1\;-1|0\,0\rangle\,|I=0\rangle + \langle 1\,1, 1\;-1|2\,0\rangle\,|I=2\rangle\} \\
&= N\{\sqrt{\frac{1}{3}}\,|I=0\rangle + \sqrt{\frac{1}{6}}\,|I=2\rangle\} \\
\Rightarrow \langle\pi^+\pi^-|\pi^+\pi^-\rangle &= 1 \;\Rightarrow N = \sqrt{2} \\
B^C_{J\Lambda} &= \sqrt{\frac{2}{3}}B^{I=0}_{J\Lambda} + \sqrt{\frac{1}{3}}B^{I=2}_{J\Lambda}\,.
\end{aligned}$$

The same for the neutral pions $B^{\mathrm{N}}_{J\Lambda}$:

$$\begin{aligned}
|\pi^0\pi^0\rangle &= N\{\langle 1\,0, 1\,0|0\,0\rangle\,|I=0\rangle + \langle 1\,0, 1\,0|2\,0\rangle\,|I=2\rangle\} \\
&= N\{-\sqrt{\frac{1}{3}}\,|I=0\rangle + \sqrt{\frac{2}{3}}\,|I=2\rangle\} \\
\Rightarrow \langle\pi^+\pi^-|\pi^+\pi^-\rangle &= 1 \;\Rightarrow N = 1 \\
B^N_{J\Lambda} &= -\sqrt{\frac{1}{3}}B^{I=0}_{J\Lambda} + \sqrt{\frac{2}{3}}B^{I=2}_{J\Lambda}\,.
\end{aligned}$$

These expressions can be solved for the isospin partial waves:

$$B^{I=0}_{J\Lambda} = \sqrt{\frac{2}{3}}B^C_{J\Lambda} - \sqrt{\frac{1}{3}}B^N_{J\Lambda}\,, \quad B^{I=2}_{J\Lambda} = \sqrt{\frac{1}{3}}B^C_{J\Lambda} + \sqrt{\frac{2}{3}}B^N_{J\Lambda}\,. \tag{7.14}$$

Note that because photons do only couple to the charge, the neutral Born partial waves $B^N_{J\Lambda}$ are zero.

7.5.2 Phase Shifts for the $\pi\pi$ scattering

The phase-shifts δ^{ij}, taken from [24], are shown in Fig. 7.17. One can see, that the $B^{0,++}_{00}$ and $B^{0,00}_{00}$ partial waves will change most by unitarization, because the δ^{00} has, going up to π-radians, by far the highest amplitude.

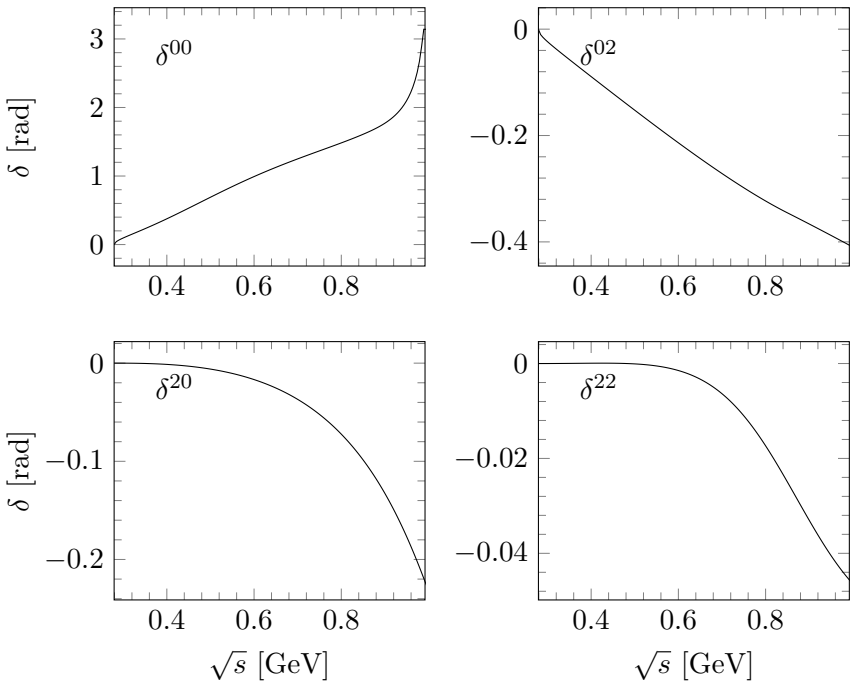

Figure 7.17: $\pi\pi \to \pi\pi$ scattering phase shifts taken from [24].

7.5.3 Unitarization Procedure

To apply the techniques from Chapter 5 to the Born amplitudes, the phase shifts are in principle needed up to infinity. Fortunately, the effect of the unitarization is dominated by the low-energy behaviour of the phase-shifts. This lead to the choice to evaluate the integrals in the formula for the Omnès function and the dispersion relation up to the kaon-threshold and to neglect the contribution of the rest of the integration.

The procedure is as follows: First, the Omnès functions are calculated using (5.1). The threshold here is $s_0 = 4m_\pi^2$. Then, the partial waves are decomposed into isospins, see section 7.5.1, where $B_{J\Lambda} \equiv B^{\mathrm{C}}_{J\Lambda}$. The partial waves $B^I_{J\Lambda}$ from Eq. (7.14) are then unitarized using (5.2).

The resulting $\gamma^*\gamma^* \to \pi^+\pi^-$ partial waves $F_{J\Lambda} \equiv F^{\mathrm{C}}_{J\Lambda}$ are shown in Fig. 7.18. As discussed in the previous section, the F_{00} wave changes most by unitarization. It is higher than the Born amplitude at low energies and lower at high energies. The change of the other waves is small.

The unitarized full amplitude is obtained by first subtracting the Born S and D waves from the Born amplitude and then adding the unitarized S and D waves. The most prominent change, coming from the S waves, F^{++}_{00} and F^{00}_{00}, can be seen as a shift of the whole curve in the differential cross sections, Fig. 7.19. As far as one can tell from the Mark II data points [20], there seems to be a clear tendency that the $\gamma\gamma \to \pi^+\pi^-$ unitarized curve is in better agreement than the Born curve. Further

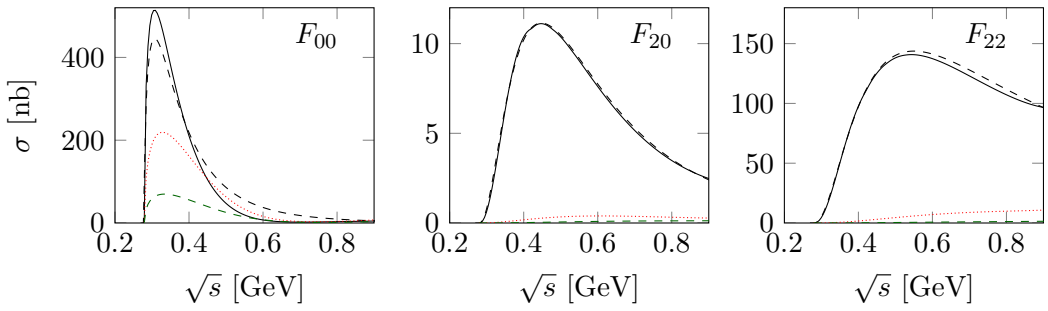

Figure 7.18: $\gamma\gamma \to \pi^+\pi^-$ unitarized partial waves (solid-black line), $\gamma^*\gamma \to \pi^+\pi^-$ with $Q^2 = 0.5\,\mathrm{GeV}^2$ (dotted-red line), and $\gamma^*\gamma^* \to \pi^+\pi^-$ with $Q_1^2 = Q_2^2 = 0.5\,\mathrm{GeV}^2$ (dashed-green line). $\gamma\gamma \to \pi^+\pi^-$ Born (dashed-black line).

measurements, e. g. at BES III [25], should be able to unambiguously differentiate between them.

The integrated $\gamma\gamma \to \pi^+\pi^-$ cross section, Fig. 7.20, shows also the difference between Born and unitarized amplitudes, so even without the knowledge of angular dependence, the rescattering effects are visible.

The BES III detector has an acceptance of $|\cos\theta| \leq 0.93$ [25]. The corresponding integrated cross section, Fig. 7.21, seems to be high enough, that the $\gamma^*\gamma \to \pi^+\pi^-$ and $\gamma^*\gamma^* \to \pi^+\pi^-$ for $Q_1^2 = Q_2^2 = 0.5\,\mathrm{GeV}^2$ can be measured with high precision, so that one can distinguish between Born and unitarized wave.

Before finishing the discussion, the neutral channel $\gamma\gamma \to \pi^0\pi^0$ shall be discussed. In this process, the important effect is, that even though there is no Born contribution to $\gamma\gamma \to \pi^0\pi^0$, the creation of neutral pions by $\pi\pi \to \pi\pi$ rescattering is included through unitarization, see Fig. 7.22. At low energies, the Crystal Ball data [26] is in good agreement with the unitarized curve. The deviations at higher energies will not be discussed here.

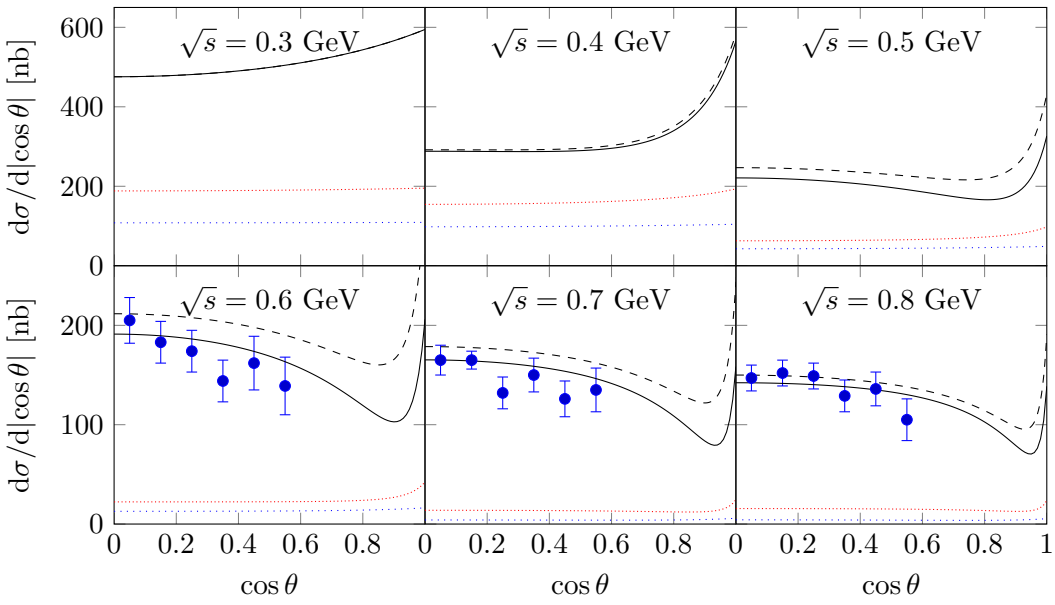

Figure 7.19: $\gamma\gamma \to \pi^+\pi^-$ cross section with S and D unitarized waves (solid-black line). $\gamma^*\gamma \to \pi^+\pi^-$ cross section for $Q^2 = 0.5\mathrm{GeV}^2$ with S and D unitarized waves (dotted-red line), $\gamma^*\gamma^* \to \pi^+\pi^-$ cross section for $Q_1^2 = Q_2^2 = 0.5\mathrm{GeV}^2$ (dotted-blue line). For comparison, the $\gamma\gamma \to \pi^+\pi^-$ Born cross section is shown (black-dashed line). Experimental $\gamma\gamma \to \pi^+\pi^-$ data from Mark II [20].

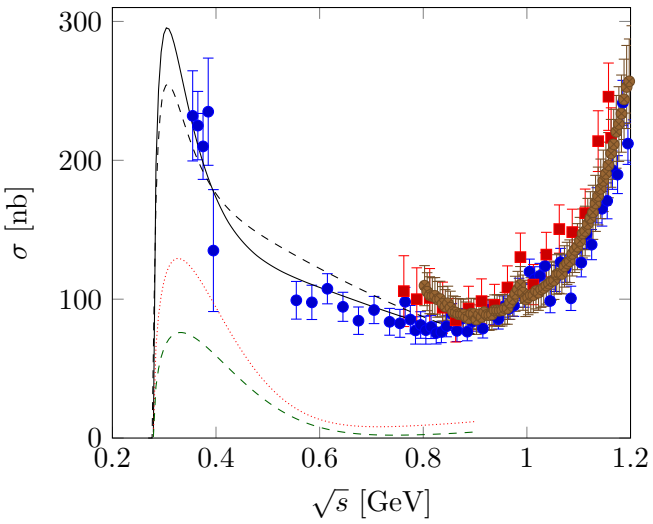

Figure 7.20: $\gamma\gamma \to \pi^+\pi^-$ cross section ($|\cos\theta| < 0.6$) with S and D unitarized waves (solid-black line), $\gamma^*\gamma \to \pi^+\pi^-$ with $Q^2 = 0.5\text{GeV}^2$ (dotted-red line), and $\gamma^*\gamma^* \to \pi^+\pi^-$ $Q_1^2 = Q_2^2 = 0.5\text{GeV}^2$ (dashed-green line). $\gamma\gamma \to \pi^+\pi^-$ Born cross section (black-dashed line). Experimental $\gamma\gamma \to \pi^+\pi^-$ data from Mark II [20] (blue dots), Cello [21] (red squares) and Belle [22] (brown dots).

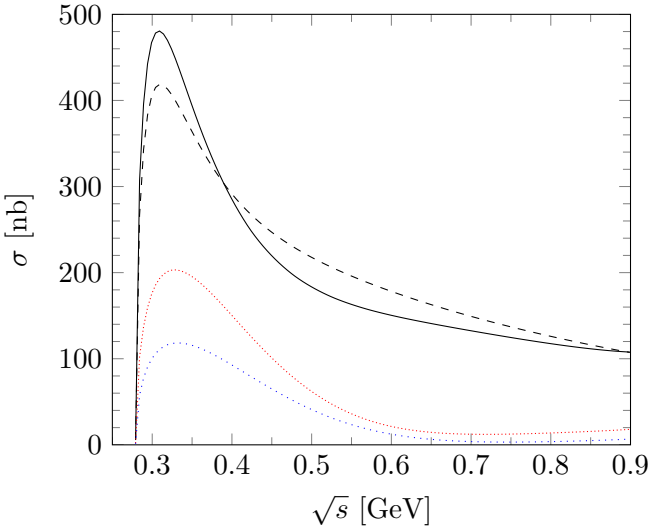

Figure 7.21: $\gamma\gamma \to \pi^+\pi^-$ cross section ($|\cos\theta| < 0.93$) with S and D unitarized waves (solid-black line), $\gamma^*\gamma \to \pi^+\pi^-$ with $Q^2 = 0.5\text{GeV}^2$ (dotted-red line), and $\gamma^*\gamma^* \to \pi^+\pi^-$ $Q_1^2 = Q_2^2 = 0.5\text{GeV}^2$ (dashed-green line). $\gamma\gamma \to \pi^+\pi^-$ Born cross section (black-dashed line).

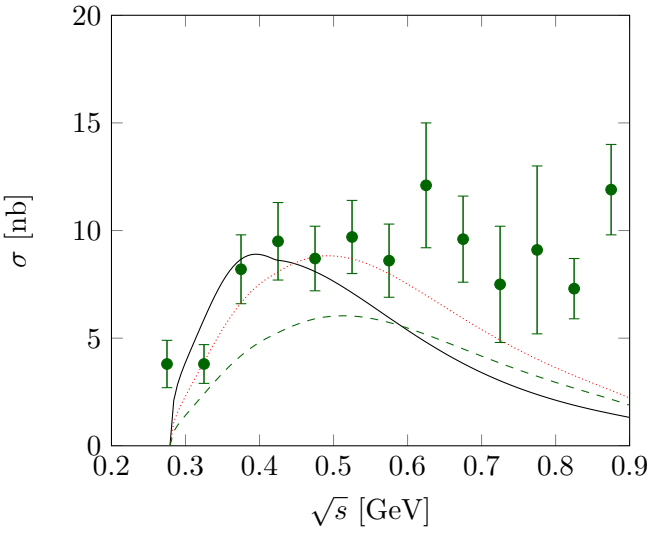

Figure 7.22: $\gamma\gamma \to \pi^0\pi^0$ cross section ($|\cos\theta| < 0.8$)with S and D unitarized waves (solid-black line), $\gamma^*\gamma \to \pi^0\pi^0$ with $Q^2 = 0.5\,\mathrm{GeV}^2$ (dotted-red line), and $\gamma^*\gamma^* \to \pi^0\pi^0$ $Q_1^2 = Q_2^2 = 0.5\,\mathrm{GeV}^2$ (dashed-green line). $\gamma\gamma \to \pi^0\pi^0$ Born cross section (black-dashed line). Experimental $\gamma\gamma \to \pi^0\pi^0$ data from Crystal Ball [26] (green dots).

8 Summary and Outlook

The experimental results for the muon anomalous magnetic moment shows a three standard deviation discrepancy with the current Standard Model calculations. From the theory side, the main error is coming from the hadronic contribution, mainly by the hadronic light-by-light scattering contribution, which cannot be linked to any cross section and one relies on well-educated models to account for it. The pseudoscalar exchange contribution is the dominant piece in the hadronic light-by-light scattering contribution and the pion loop the subdominant. Since this piece is less known, it is the main object of this thesis. Dispersion relations relate the pion-loop to the $\gamma\gamma \to \pi\pi$ process for which data is available.

Starting from a scalar quantum-electrodynamic Lagrangian, the Born diagrams for the process $\gamma\gamma \to \pi\pi$ have been derived and evaluated for real and virtual photons. The required corrections of the coupling between virtual photons and pions have been accounted for by a form factor. The results have been used to construct the imaginary part of the $\gamma\gamma \to \gamma\gamma$ amplitude using the optical theorem. The $\gamma^*\gamma^* \to \pi\pi$ amplitude has been tuned by including rescattering of the pions in the final state through unitarization of the S and D partial waves. This effect has been shown to be a major improvement and the resulting cross section provides a good description of the data up to the kaon production threshold. The result will be used to help analyze the BES III data [25] and contribute to the understanding of $\gamma^*\gamma^* \to \pi\pi$ as an important part of the hadronic light-by-light scattering contribution to the muon anomalous magnetic moment.

Beyond the $\gamma\gamma \to \pi\pi$ channel (where the appropriate theoretical errors are still to be incorporated), the two-kaon channel contribution together with the resonance formation (the tensor-meson $f_2(1270)$, the scalar-mesons $f_0(980)$ and $f_0(500)$), the four-pion channel and the pion polarizabilities deserve attention and should be the focus of a future work.

A Appendix

A.1 Formulas

The formulas in this section are taken from [15].

Dimensional Regularization

$$\int \frac{d^d l}{(2\pi)^d} \frac{1}{(l^2-\Delta)^n} = \frac{(-1)^n \imath}{(4\pi)^{d/2}} \frac{\Gamma(n-d/2)}{\Gamma(n)} \left(\frac{1}{\Delta}\right)^{n-d/2}$$

$$\int \frac{d^d l}{(2\pi)^d} \frac{l^\mu l^\nu}{(l^2-\Delta)^n} = \frac{(-1)^{n-1} \imath}{(4\pi)^{d/2}} \frac{g^{\mu\nu}}{2} \frac{\Gamma(n-d/2-1)}{\Gamma(n)} \left(\frac{1}{\Delta}\right)^{n-d/2-1}$$

$$\int \frac{d^d l}{(2\pi)^d} \frac{l^\mu l^\nu l^\rho l^\sigma}{(l^2-\Delta)^n} = \frac{(-1)^n \imath}{(4\pi)^{d/2}} \frac{\Gamma(n-d/2-2)}{\Gamma(n)} \left(\frac{1}{\Delta}\right)^{n-d/2-2} \times \left(g^{\mu\nu}g^{\rho\sigma} + g^{\mu\rho}g^{\nu\sigma} + g^{\mu\sigma}g^{\nu\rho}\right) \frac{1}{4}$$

$$\int \frac{d^d l}{(2\pi)^d} \frac{\text{odd \# of } l\text{s}}{(l^2-\Delta)^n} = 0$$

for $d \approx 4$ is

$$\left(\frac{1}{\Delta}\right)^{2-d/2} = 1 - (2 - \frac{d}{2}) \ln(\Delta) + \cdots$$

for $x \approx 0$ is

$$\Gamma(x) = \frac{1}{x} - \gamma_E + \mathcal{O}(x) \ , \quad \gamma_E \approx 0.5772$$

Feynman Parameters

$$\frac{1}{A_1 A_2 \cdots A_n} = \int_0^1 dx_1 \cdots dx_n \, \delta\left(\sum x_i - 1\right) \frac{(n-1)!}{[x_1 A_1 + x_2 A_2 + \cdots + x_n A_n]^n} \tag{A.1}$$

Other Formulas

$$\int dx \frac{1}{\Delta \pm \imath\epsilon} = \fint \frac{1}{\Delta} \mp \imath\pi \int dx \, \delta(\epsilon)$$

The next formula is taken from [27]:

$$\delta(f(x)) = \sum_i \frac{\delta(x - x_i)}{f'(x_i)} \tag{A.2}$$

where x_i are the zeros of f.

Bibliography

[1] W. Gerlach, O. Stern. *Z. Phys.* 8 (1924), p. 110.

[2] Paul A.M. Dirac. "The Quantum theory of electron". *Proc.Roy.Soc.Lond.* A117 (1928), pp. 610–624.

[3] Julian Schwinger. "On Quantum-Electrodynamics and the Magnetic Moment of the Electron". *Phys. Rev.* 73 (4 Feb. 1948), pp. 416–417. DOI: 10.1103/PhysRev.73.416. URL: http://link.aps.org/doi/10.1103/PhysRev.73.416.

[4] Tatsumi Aoyama et al. "Complete Tenth-Order QED Contribution to the Muon $g-2$". *Phys. Rev. Lett.* 109 (11 Sept. 2012), p. 111808. DOI: 10.1103/PhysRevLett.109.111808.

[5] M. Davier et al. "Reevaluation of the hadronic contributions to the muon $g-2$ and to $\alpha(M_Z^2)$". English. *The European Physical Journal C* 71.1 (2011), pp. 1–13. ISSN: 1434-6044. DOI: 10.1140/epjc/s10052-010-1515-z. URL: http://dx.doi.org/10.1140/epjc/s10052-010-1515-z.

[6] T. Teubner et al. "Update of $g-2$ of the Muon and Delta Alpha". *Chin.Phys.* C34 (2010), pp. 728–734. DOI: 10.1088/1674-1137/34/6/019. arXiv:1001.5401 [hep-ph].

[7] Fred Jegerlehner and Andreas Nyffeler. "The Muon $g-2$". *Phys.Rept.* 477 (2009), pp. 1–110. DOI: 10.1016/j.physrep.2009.04.003. arXiv:0902.3360 [hep-ph].

[8] Andrzej Czarnecki, William J. Marciano, and Arkady Vainshtein. "Refinements in electroweak contributions to the muon anomalous magnetic moment". *Phys. Rev. D* 67 (7 Apr. 2003), p. 073006. DOI: 10.1103/PhysRevD.67.073006. URL: http://link.aps.org/doi/10.1103/PhysRevD.67.073006.

[9] G.W. Bennett et al. "Final Report of the Muon E821 Anomalous Magnetic Moment Measurement at BNL". *Phys.Rev.* D73 (2006), p. 072003. DOI: 10.1103/PhysRevD.73.072003. arXiv:hep-ex/0602035 [hep-ex].

[10] R. Carey, K. Lynch, J. Miller, B. Roberts, W. Morse, et al. (2009).

[11] Eduardo de Rafael. "Hadronic contributions to the muon g-2 and low-energy QCD". *Phys.Lett.* B322 (1994), pp. 239–246. DOI: 10.1016/0370-2693(94)91114-2. arXiv:hep-ph/9311316 [hep-ph].

[12] R. de L. Kronig. "On the Theory of Dispersion of X-Rays". *J. Opt. Soc. Am.* 12.6 (June 1926), pp. 547–556. DOI: 10.1364/JOSA.12.000547. URL: http://www.opticsinfobase.org/abstract.cfm?URI=josa-12-6-547.

[13] H. A. Kramers. "La diffusion de la lumiere par les atomes". *Atti. congr. intern. fisici* 2 (1927), pp. 545–557.

[14] I.N. Bronstein and K.A. Semendjajew. *Taschenbuch der Mathematik*. Harri Deutsch, 2008. ISBN: 9783817120079.

[15] M.E. Peskin and D.V. Schroeder. *An Introduction To Quantum Field Theory*. Advanced Book Program. Addison-Wesley Publishing Company, 1995. ISBN: 9780201503975.

[16] Jun J. Sakurai. *Modern quantum mechanics*. Rev. ed. Reading, Mass.: Addison-Wesley, 1994, X, 500 S. ISBN: 0-201-53929-2.

[17] D. Drechsel et al. "Fixed t subtracted dispersion relations for Compton Scattering off the nucleon". *Phys.Rev.* C61 (1999), p. 015204. DOI: 10.1103/PhysRevC.61.015204. arXiv:hep-ph/9904290 [hep-ph].

[18] R. Omnes. "On the Solution of certain singular integral equations of quantum field theory". *Nuovo Cim.* 8 (1958), pp. 316–326. DOI: 10.1007/BF02747746.

[19] B. Moussallam. "Unified dispersive approach to real and virtual photon-photon scattering at low energy" (2013). arXiv:1305.3143 [hep-ph].

[20] J. Boyer et al. "Two-photon production of pion pairs". *Phys. Rev. D* 42 (5 Sept. 1990), pp. 1350–1367. DOI: 10.1103/PhysRevD.42.1350. URL: http://link.aps.org/doi/10.1103/PhysRevD.42.1350.

[21] Jens Harjes. "Experimentelle Untersuchung der Reaktion $\gamma\gamma \to \pi^+\pi^-$ mit dem Detektor CELLO" (1991).

[22] T. Mori et al. "High Statistics Measurement of the Cross Sections of $\gamma\gamma \to \pi^+\pi^-$ Production". *Journal of the Physical Society of Japan* 76.7 (2007), p. 074102. DOI: 10.1143/JPSJ.76.074102. URL: http://jpsj.ipap.jp/link?JPSJ/76/074102/.

[23] J. Beringer et al. (Particle Data Group). *PR D 010001* 86 (2012), and 2013 partial update for the 2014 edition. URL: http://pdg.lbl.gov.

[24] R. García-Martín et al. "Pion-pion scattering amplitude. IV. Improved analysis with once subtracted Roy-like equations up to 1100 MeV". *Phys. Rev. D* 83 (7 Apr. 2011), p. 074004. DOI: 10.1103/PhysRevD.83.074004. URL: http://link.aps.org/doi/10.1103/PhysRevD.83.074004.

[25] D.M. Asner et al. "Physics at BES-III". *Int.J.Mod.Phys.* A24 (2009), S1–794. arXiv:0809.1869 [hep-ex]; Achim Denig and Yuping Guo. private communication.

[26] H. Marsiske et al. "Measurement of $\pi^0\pi^0$ production in two-photon collisions". *Phys. Rev. D* 41 (11 June 1990), pp. 3324–3335. DOI: 10.1103/PhysRevD.41.3324. URL: http://link.aps.org/doi/10.1103/PhysRevD.41.3324.

[27] Wikipedia. *Delta-Distribution — Wikipedia, Die freie Enzyklopdie*. [Online; Stand 8. April 2013]. 2013. URL: http://de.wikipedia.org/w/index.php?title=Delta-Distribution&oldid=116810032.